Experimental determination of rolling element bearing stiffness

Knaapen, R.J.W.

Award date:
1999

EXPERIMENTAL DETERMINATION OF ROLLING ELEMENT BEARING STIFFNESS

R.J.W. KNAAPEN

WFW-REPORT 97.017

Graduation report

Eindhoven University of Technology
Faculty of Mechanical Engineering
Department of Engineering Dynamics

Supervised by:
Ir. L. Kodde
Dr. ir. A. de Kraker

Examination committee:
Prof. dr. ir. D.H. van Campen
Prof. dr. ir. J.W. Verheij
Dr. ir. A. de Kraker
Ir. L. Kodde

Eindhoven
March 18, 1997

Experimental Determination of Rolling Element Bearing Stiffness

R.J.W. Knaapen

March 18, 1997

Abstract

To predict the vibration in rotating mechanical equipment, the role of bearings as a dynamic coupler between the shaft and casing must be completely understood. In 1990, Lim and Singh have presented a bearing stiffness model with three translational and three rotational degrees of freedom, to replace previous models, which, in general, neglect flexural or out-of-plane type vibrations. This model is characterized graphically in order to enhance the understanding of the influence of the contact angle and preloads. Earlier attempts to measure all stiffnesses of a bearing for comparison with the model partly failed, because the experimental setup had some special shortcomings. The use of more complex identification methods could not overcome the problems. A modified experimental setup is presented, which is capable of yielding reproducible measurements. Estimating a complete stiffness matrix directly from the measured transfer matrix appeared to be unfeasible. Therefore, single-degree-of-freedom fits on the measurements are compared with fits on the model. However, the so-called coupling terms cannot be compared using SDOF fit procedures. Nevertheless, these results appear to be very promising and applicable in practice, but future research is needed to investigate the difference between the measured stiffnesses and the model stiffnesses. In addition to stiffnesses, the fit procedures yield damping values as well, which unjustify the use of Rayleigh damping. Finally, matters such as hysteresis, reproducibility and reciprocity are investigated.

Samenvatting

Het voorspellen van trillingen in machines met draaiende elementen vereist een grondige kennis van lagers als dynamische koppeling tussen de as en de behuizing. Daartoe hebben Lim en Singh in 1990 een lagermodel geïntroduceerd met drie translatie- en drie rotatievrijheidsgraden, in plaats van voorgaande modellen, die over het algemeen de buigtrillingen van de as of de transversale trillingen van de behuizing buiten beschouwing laten. Een aantal modelkarakteristieken wordt beschouwd ten behoeve van het inzicht in verschijnselen zoals contacthoeken en voorspanningen. Voorheen is het niet volledig gelukt om de stijfheden van een lager te meten en te vergelijken met het model, vanwege een aantal gebreken in de proefopstelling. Het gebruik van complexere identificatiemethoden kon hieraan niets bijdragen. Daarom is een gewijzigde opstelling gerealiseerd die reproduceerbare meetgegevens kan leveren. Het schatten van een complete stijfheidsmatrix bleek echter ondoenlijk. Daarom zijn er een-graad-van-vrijheid fits uitgevoerd op de gemeten overdrachtsfuncties en het model, welke nadien met elkaar worden vergeleken. De zogenaamde kruistermen echter, zijn op deze manier niet te vergelijken. Desalniettemin lijken deze resultaten veelbelovend en in de praktijk toepasbaar, maar er is nog onderzoek nodig om het verschil tussen het model en de experimenten te kunnen verklaren. Buiten stijfheden leveren de fit-procedures ook dempingsresultaten, die het gebruik van Rayleigh-demping in het model afkeuren. Tenslotte is er gekeken naar verschijnselen zoals hysterese, reproduceerbaarheid en reciprociteit.

Science is built up of facts, as a house is built of stones, but an accumulation of facts is no more a science than a heap of stones is a house.

Jules-Henri Poincaré, Science and Hypothesis

Contents

List of Figures

List of Symbols

Chapter 2

A_0	$[m]$	Unloaded distance between the inner and outer raceway groove curvature centers
A_j	$[m]$	Loaded distance between the inner and outer raceway groove curvature centers
F	$[N]$	Force
K_n	$[N/m^n]$	Rolling element load-deflection stiffness constant
M	$[Nm]$	Moment
n	$[-]$	Bearing type exponent
Q_j	$[N]$	Resultant normal load on the j-th rolling element
r_j	$[m]$	Radial distance to inner raceway groove curvature centre
r_L	$[m]$	Radial clearance
$\{q\}_{bm}$		Mean bearing displacement
α_0	$[rad]$	Unloaded contact angle
α_j	$[rad]$	Loaded contact angle
β	$[rad]$	Rotation
δ	$[m]$	Displacement
δ^*	$[m]$	Displacement
Ψ_j	$[rad]$	Angular location of j-th rolling element

Chapter 3

A	$[m^2]$	Cross sectional area
E	$[N/m^2]$	Young's modulus
I	$[m^4]$	Bending moment of inertia
k	$[N/m]$	Stiffness
K	$[N/m]$	Stiffness
l	$[m]$	Length
m	$[kg]$	Mass
$p(x)$	$[N/m]$	Load distribution
$s(t)$	$[m]$	Displacement
t	$[s]$	Time
$w(x,t)$	$[m]$	Displacement

x	$[m]$	Coordinate
$y(x)$	$[-]$	Eigenmode shape
ρ	$[kg/m^3]$	Density
ρ_l	$[kg/m]$	Density per unit length

Chapter 4

$\underline{A_i}$		Least Squares system matrix of i-th measurement
$\underline{A}$		Total Least Squares system matrix
$\underline{B}$		Damping matrix
$\underline{\widehat{B}}$		Damping matrix estimate
D_i		Theoretical transfer amplitude
$\underline{E}$		Total Least Squares system matrix
f	$[N]$	Force
$\widehat{f}$	$[N]$	Force amplitude
$\underline{H}$		Transfer function
i	$[-]$	Sample number
$\underline{I}$		Identity matrix
$\underline{K}$		Stiffness matrix
$\underline{\widehat{K}}$		Stiffness matrix estimate
$\underline{M}$		Mass matrix
$\underline{\widehat{M}}$		Mass matrix estimate
P_k		Participation factor for mode k
q	$[m]$	Displacement
$\widehat{q}$	$[m]$	Displacement amplitude
$\underline{S_i}$		Error matrix of i-th measurement
$\underline{S}$		Total error matrix
$\underline{V}$		Instrumental Variables matrix
$\underline{X}$		Unknown matrix
$\underline{\widehat{X}}$		Unknown matrix extimate
$\underline{Z}$		Dynamic stiffness
ε_i		Error
ξ_k	$[-]$	Damping factor for mode k
ω	$[rad/s]$	Frequency
Ω_k	$[rad/s]$	Eigenfrequency for mode k

Subscripts

a	Auxiliary
e	Experimental
i	Concerning the i-th sample
iv	Instrumental Variables
j	Concerning the j-th rolling element
k	Concerning mode k
ls	Least Squares
rj	Radial direction, rolling element j
zj	Axial direction, rolling element j
t	Theoretical
xbm	Mean bearing displacement in x-direction
ybm	Mean bearing displacement in y-direction
zbm	Mean bearing displacement in z-direction
xm	Mean displacement in x-direction
ym	Mean displacement in y-direction
zm	Mean displacement in z-direction

Chapter 1

Introduction

Noise and vibration generated by rotating mechanical equipment have always been a problem in the implementation of new technology in automobiles, rotorcrafts and industrial machines. Recently, the need for reliable vibration prediction methods have been found to be crucial as faster and lighter machines are being designed. In most of these rotating systems, the vibration transmission through bearings, which support the rotating shafts on flexible or rigid casings, is dominant. Hence, in order to obtain a reliable mathematical model of the overall dynamic system, a complete understanding of the vibration transmission mechanism through bearings, and the role of bearings as a dynamic coupler between the shaft and casing, is essential.

In the past, bearing models were able to describe only purely in-plane type motions. In subsequent research however, experimental results have shown that the case plate motion is primarily flexural or out-of-plane type. In 1990, Lim and Singh have presented a bearing stiffness model in which three translational and three rotational degrees of freedom are used [1]. This model is improved for roller bearings by Van Roosmalen in 1994 by taking a non-uniform load distribution on the line contact between the inner race, roller and outer race of the bearing [4].

The model, which consists of a set of non-linear equations, can be numerically solved using the computer program `Lager`, which results in a theoretical bearing stiffness matrix [5]. In previous research, attempts are made to experimentally determine the bearing stiffness matrix. Well designed experimental setups [3] and identification algorithms [2] could not yet sufficiently overcome the non-reproducibility of the measurements and the inaccuracy in the torque stiffnesses. Applying higher preloads was thought to be the best solution to this problem, as in practice no rolling element is allowed to come loose.

The purpose of this research is to develop an experimental setup by which a total bearing stiffness matrix can be measured, without the occurrence of non-reproducibility and with high accuracy in the rotational stiffnesses. Subsequently, the experimentally determined stiffness can be compared to the theoretical model which gives a decisive answer to the question whether the model is suitable for the accurate prediction of rolling element bearing stiffnesses, used for vibration prediction purposes.

Chapter 2

The Bearing Model

Often, rotor dynamic models describe rolling element bearings as purely translational stiffness elements. This approach, however, will be inadequate in the explanation of the vibration transmission from the shaft to the casing. Such models can only predict purely in-plane-type motion on the flexible casing plate given only the bending motion on the shaft. However, experimental results have shown that the casing plate motion is primarily flexural or out-of-plane type. Therefore, Lim et. al. developed an extended bearing model in which both the translational and rotational degrees of freedom are taken into account. As this results in six degrees of freedom, the bearing stiffness will be expressed by means of a 6×6 stiffness matrix. The presented model determines stiffness matrices of deep groove ball bearings as well as angular contact ball bearings, straight roller bearings and taper roller bearings under the following assumptions.

2.1 Assumptions

- Ball bearings have elliptical contacts and roller types have rectangular contacts between the inner race, rolling elements and outer race when loaded.
- The loaded contact angles α_j of the ball types may change, but α_j in the roller type remains relatively constant.
- Each bearing is characterized by its kinematic and design parameters, such as:
  - the unloaded contact angle α_0,
  - the radial clearance r_L,
  - the effective stiffness coefficient K_n for inner ring-single rolling element-outer ring contacts,
  - preloads,
  - radius of inner raceway groove curvature centre for ball type and bearing pitch radius for roller type.
- The mean bearing displacements as shown in Figure 2.1 are given by the relative rigid body motions between the inner and outer rings.

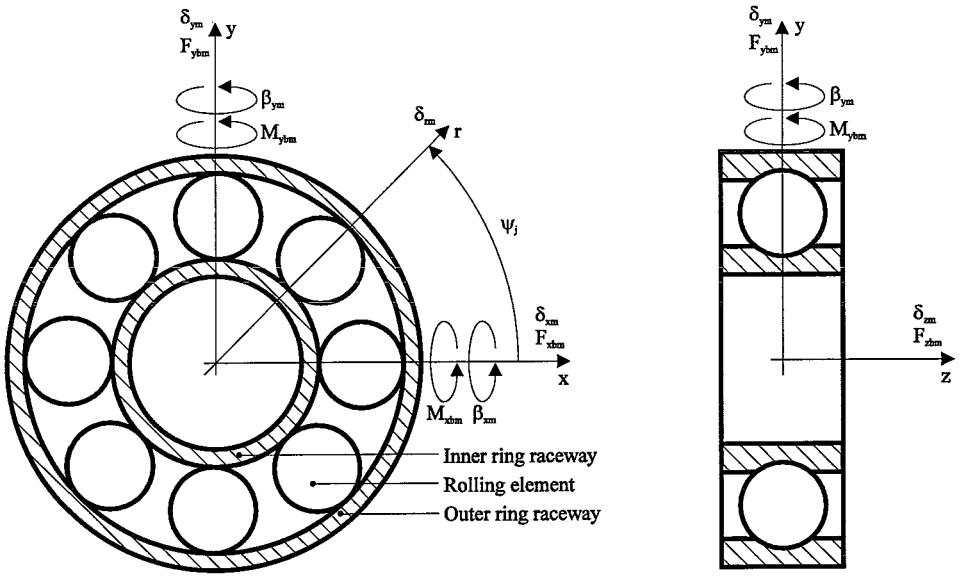

Figure 2.1: Rolling element bearing kinematics and coordinate system

- The vibrations initiated by the rotation of the shaft are neglected with respect to the steady state deflection of the bearing. Applying high preloads will justify this assumption as well as the non-rotating shaft in the experimental setup.
- The basic load-deflection relation for each elastic rolling element is defined by Hertzian contact stress theory, and the load experienced by each rolling element is described by its relative location in the bearing raceway.
- Due to the cages, the position of each rolling element relative to one another is always maintained.
- Secondary effects such as centrifugal forces and gyroscopic moments on the bearing are ignored as these effects only evolve at extremely high rotational speeds.
- Tribological issues are not taken into account. Damping is assumed to be proportional to the stiffness, thus Rayleigh damping is used in the bearing motion simulations.
- It is obvious that rotations in z-direction will have zero stiffness. Consequently, the resulting stiffness matrix will contain 5×5 effective elements.

2.2 Bearing load-displacement relations

In this section, the relation between the bearing forces $\{ F_{xbm} \quad F_{ybm} \quad F_{zbm} \}$ and moments $\{ M_{xbm} \quad M_{ybm} \}$ transmitted through the rolling element bearing, and the bearing displacements $\{q\}_{bm}$ as given in Figure 2.1 will be outlined.

The bearing displacements $\{q\}_{bm}$ are used to derive the resultant elastic deformation $\delta(\Psi_j)$ of the j-th rolling element located at angle Ψ_j from the x-axis. From the elastic deformation

of the ball bearing in Figure 2.2, $\delta(\Psi_j)$ is

$$\delta(\Psi_j) = \begin{cases} A(\Psi_j) - A_0 & ,\delta_j > 0 \\ 0 & ,\delta_j \leq 0 \end{cases} \tag{2.1}$$

$$A(\Psi_j) = \sqrt{(\delta^*)_{zj}^2 + (\delta^*)_{rj}^2} \tag{2.2}$$

$$(\delta^*)_{zj} = A_0 \sin\alpha_0 + (\delta)_{zj} \tag{2.3}$$

$$(\delta^*)_{rj} = A_0 \cos\alpha_0 + (\delta)_{rj} \tag{2.4}$$

where A_0 and A are the unloaded and loaded relative distances between the inner a_i and outer a_o raceway groove curvatures centres. In Equation 2.1, the effective j-th rolling element displacements in the axial $(\delta)_{zj}$ and radial $(\delta)_{rj}$ directions are given in Figure 2.3 in terms of the bearing displacements $\{q\}_{bm}$.

$$(\delta)_{zj} = \delta_{zm} + r_j\left(\beta_{xm}\sin(\Psi_j) - \beta_{ym}\cos(\Psi_j)\right) \tag{2.5}$$

$$(\delta)_{rj} = \delta_{xm}\cos(\Psi_j) + \delta_{ym}\sin(\Psi_j) - r_L \tag{2.6}$$

where r_j is the radial distance of the inner raceway groove curvature centre. The load-deflection relationship for a single rolling element according to the Hertzian contact stress principle can be stated as

$$Q_j = K_n\delta_j^n \tag{2.7}$$

where Q_j is the resultant normal load on the rolling element. In the case of elliptical contacts the exponent n is equal to $\frac{3}{2}$, for roller type bearings with rectangular contacts n is equal to $\frac{10}{9}$. The loaded contact angle α_j may alter in the ball bearing case. The sign convention is such that α_j is positive when measured from the bearing x-y plane towards the axial z-axis, and negative otherwise. For the ball bearing of Figure 2.2 the loaded contact angle α_j is

$$\tan(\alpha_j) = \frac{A_0\sin\alpha_0 + (\delta)_{zj}}{A_0\cos\alpha_0 + (\delta)_{rj}} \tag{2.8}$$

To determine the total stiffness matrix, the effects of all z rolling element stiffnesses given by $\delta_j > 0$ have to be combined. First, the bearing mean load vector $\{f\}_{bm}$ has to be related to the bearing displacement vector $\{q\}_{bm}$ through vectorial sums of Q_j in Equation 2.7 for all of the loaded rolling elements, which leads to the following bearing moments $\{M_{wbm}\}$ and forces $\{F_{wbm}\}$.

$$\begin{Bmatrix} M_{xbm} \\ M_{ybm} \\ M_{zbm} \end{Bmatrix} = \sum_j^z r_j Q_j \sin\alpha_j \begin{Bmatrix} \sin\Psi_j \\ -\cos\Psi_j \\ 0 \end{Bmatrix} \tag{2.9}$$

$$\begin{Bmatrix} F_{xbm} \\ F_{ybm} \\ F_{zbm} \end{Bmatrix} = \sum_j^z Q_j \begin{Bmatrix} \cos\alpha_j\cos\Psi_j \\ \cos\alpha_j\sin\Psi_j \\ \sin\alpha_j \end{Bmatrix} \tag{2.10}$$

Finally, a symmetric bearing stiffness matrix of dimension 6×6 can be defined as follows:

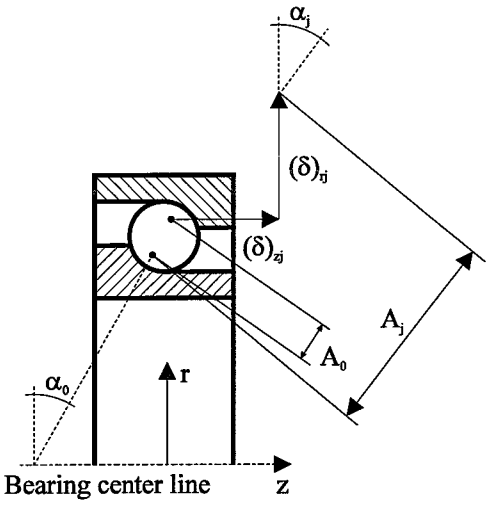

Figure~2.2: Elastic deformation of rolling element for non-constant contact angle

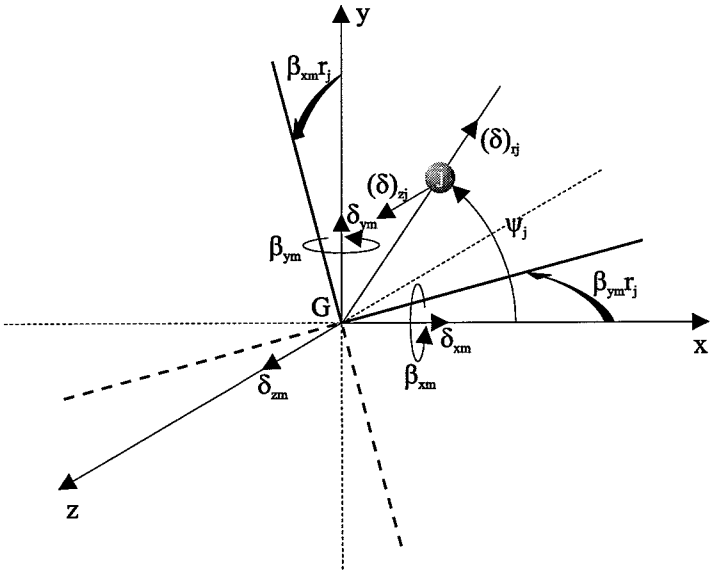

Figure~2.3: The effective deformations in terms of the mean bearing displacements $\{q\}_{bm}$

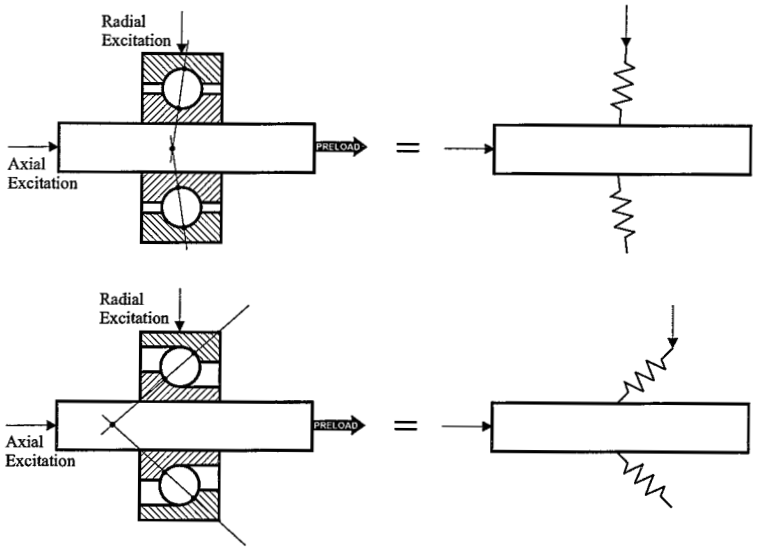

Figure 2.4: Influence of the contact angle on the radial and axial stiffness

$$\left[\begin{array}{cc} \frac{\partial F_{wbm}}{\partial \delta_{im}} & \frac{\partial F_{wbm}}{\partial \beta_{im}} \\ \frac{\partial M_{wbm}}{\partial \delta_{im}} & \frac{\partial M_{wbm}}{\partial \beta_{im}} \end{array}\right]_{\{q\}_{bm}} ; w, i = x, y, z \tag{2.11}$$

Here each stiffness coefficient must be evaluated at the mean point $\{q\}_{bm}$. The symmetry is not obvious but follows after working out Equation 2.11. The explicit terms of this symmetric matrix are mentioned extensively in [1]. The numeric calculations can be done using the program `Lager` [5] for several bearing load situations.

2.3 Model Characteristics

In this paragraph some characteristics of the model are sketched. Two bearings are considered, a normal NSK 6208 deep groove ball bearing and a fictitious NSK 6208 bearing with $\alpha_0 = 40^o$, which shows the effect of the contact angle. Both, a deep groove ball bearing and an angular contact bearing are considered here, since the same is done in Chapter 5.

The stiffness matrix of a purely axial preloaded bearing is shown in Figure 2.6 in which only the upper triangle is printed because of the symmetry of the matrix. The diagonal terms show that applying a contact angle decreases the radial stiffnesses and increases the axial and rotational stiffnesses. This is accounted for in Figure 2.4, which shows that, in case of an axial preload, an angular contact bearing has higher stiffness in axial direction and a deep groove ball bearing has higher stiffness in radial direction. Considerations on the rotational stiffness are similar to the ones on axial stiffness, however, in the rotational case not all rolling elements are loaded equally. This is outlined in Figure 2.5 in which the dark rolling elements are loaded by the inner ring.

In Figure 2.6, the only existing coupling terms (i.e. $H_{x\theta_y}$, $H_{y\theta_x}$, $H_{\theta_y x}$ and $H_{\theta_x y}$) are determined by the contact angle of the bearing, for a radial excitation is converted to a

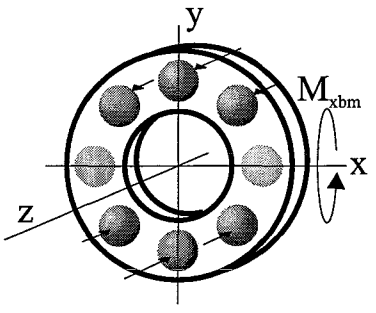

Figure~2.5: In case of a rotational load, a single rolling element 'feels' an axial load which is different for each element

momentum with resulting rotation, because of the contact angle. (See also Figure 5.5). The smaller the contact angle, the smaller is the effect of the mentioned coupling terms.

In Figure 2.7 the stiffness matrix for an increasing radial preload in y-direction combined with a constant axial preload of 800 $[N]$ is sketched. Compared to the purely axial preloaded case, four extra terms evolve, H_{yz}, $H_{z\theta_x}$, H_{zy} and $H_{\theta_x z}$. This is caused by the fact that the bearing position is no longer axi-symmetrical. This is sketched in Figure 5.11 and discussed in Section 5.3. Another difference is that some stiffnesses no longer increase or decrease monotonously. Apparently, in this case the stiffness is determined by more than one effect, in which the dominant one is determined by the combination of preloads.

The white graphs are the result of a simulation using a non-symmetric rolling element distribution. When the rolling elements were distributed symmetrically with regard to the y-z-plane, a radial preload in y-direction would not have any effect in the x-direction, and thus the white graphs would be zero. The effect of the deep groove ball bearing in the white graphs is negligible with respect to the angular contact bearing because a contact angle is needed to turn a particular load into another direction.

A very important phenomenon in the simulations is the fact that a tiny preload or disturbance can cause some matrix components to increase enormously, whereas usually they would be zero. Therefore, in practice the excitations must be exactly aimed in the right direction.

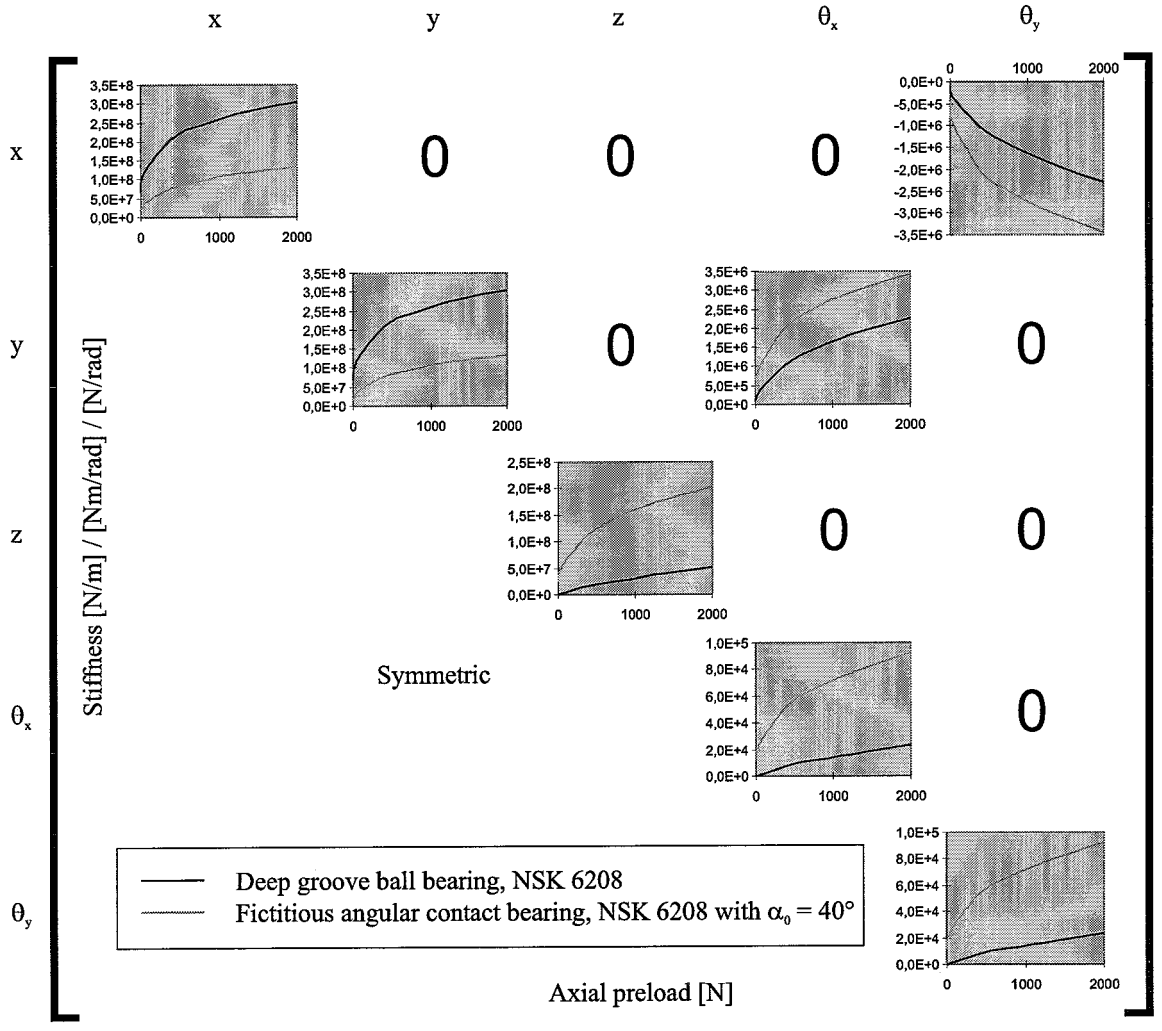

Figure 2.6: The stiffness matrix K_{bm} in case of an axial preload

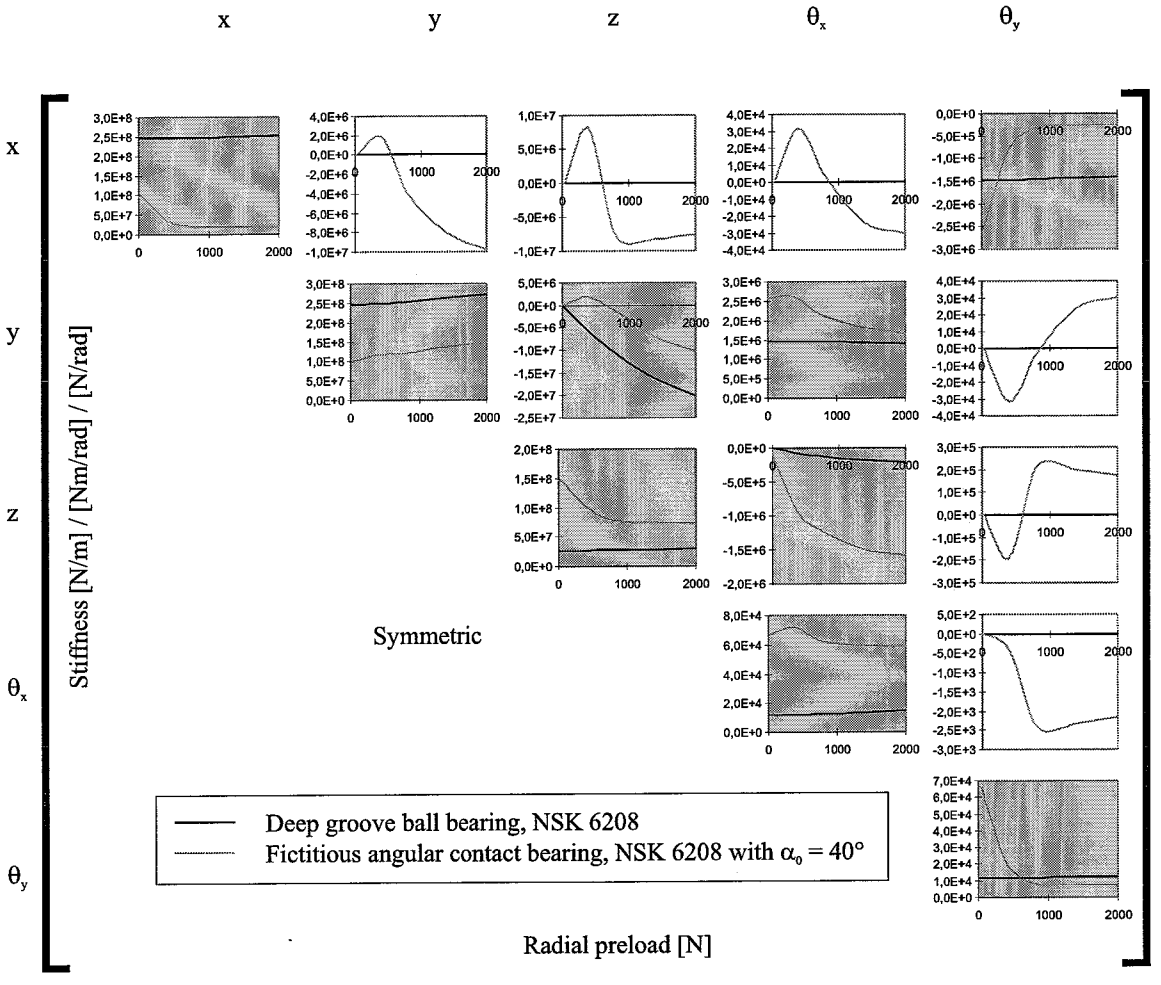

Figure 2.7: The stiffness matrix K_{bm} in case of an increasing radial preload in y-direction combined with a constant axial preload of 800 $[N]$

Chapter 3

The Experimental Setup

An experimental setup for the determination of a complete stiffness matrix is designed by Heuvelmans [3] in 1993 but measurements could not approve the theoretical bearing model, for the experimental setup suffered from non-reproducibility (see Figure 3.1). In 1995, Staps [2] performed a new set of measurements and used a Least Squares and Instrumental Variables method to identify the bearing stiffness from a transfer function. These identification algorithms were appropriate in deriving a stiffness matrix but the resulting matrix could not be matched with the theoretical model. Whether this is due to model imperfections or an experimental mismatch could not be found out. In this section a redesigned experimental setup will be presented.

3.1 Potential Problems

The new experimental setup will be dynamically excited by an excitation hammer or shaker to determine the complex transfer matrix of the bearing. However, the setup has to be in complete agreement with the assumptions stated in the previous chapter. Here, a 'stock-taking' of problems with matching solutions is presented.

One problem is the contact between the inner raceway, the rolling element and the outer raceway. In the bearing model rolling elements are allowed to come loose by neglecting their contribution to the stiffness. In practice however, the behaviour of unloaded rolling elements is hard to predict. Applying high preloads is a solution to this problem since it will force the rolling elements to make contact. Another problem is the fact that the measurements

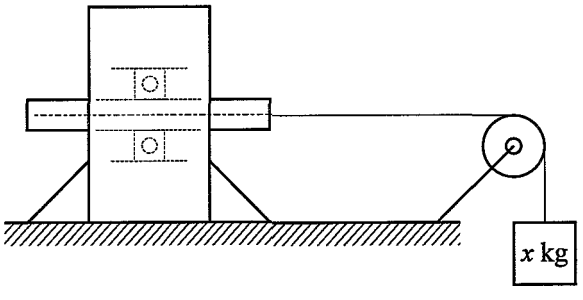

Figure 3.1: Experimental setup by Heuvelmans

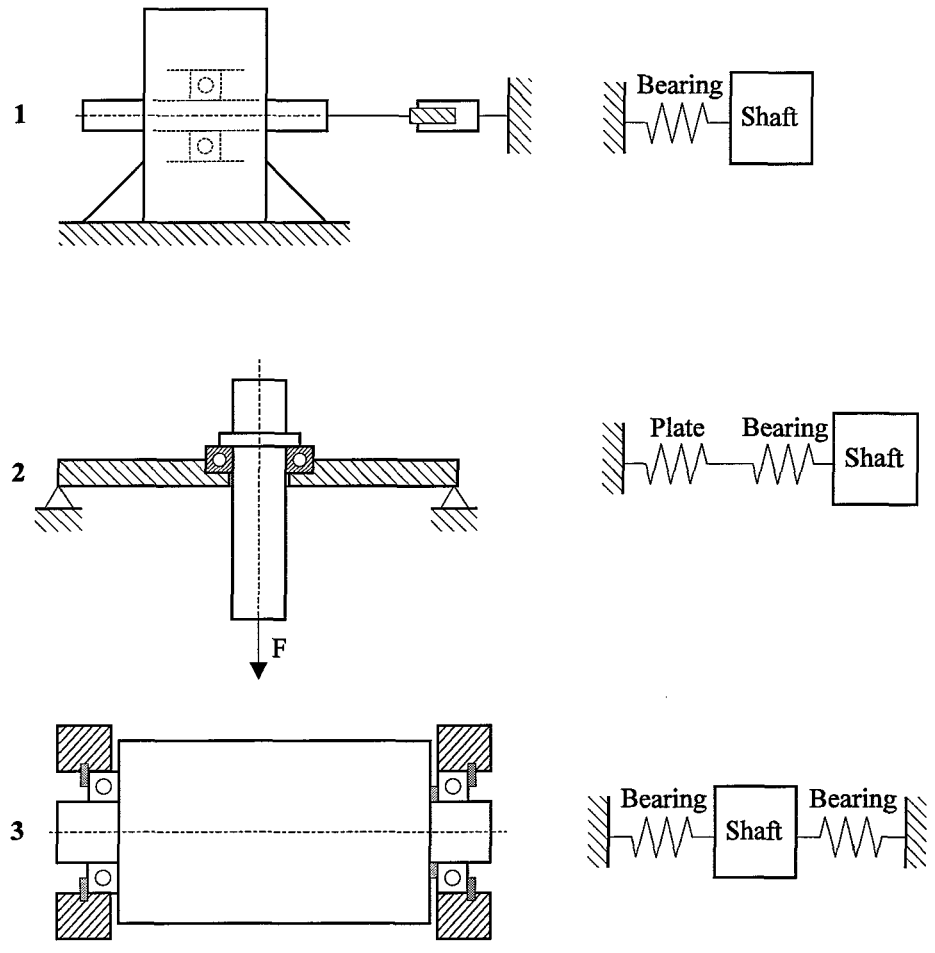

Figure~3.2: Several concepts for an experimental setup

are performed on a non-rotating shaft. Therefore, the measured transfer function could be dependent on the position of the rolling elements.

The bearing lubrication will initiate a significant and unknown amount of damping, which is, beside of the stiffness, another unknown property in the identification problem. On the other hand, the lubrication reduces the effect of unloaded rolling elements. When the shaft is excited by a shaker or excitation hammer, all parts of the experimental setup will be excited. Several eigenfrequencies will be measured which do not result from the stiffness contribution of the bearing such as vibrations in the string and the shaft itself. These effects have to be suppressed or incorporated.

3.2 The Redesign

Several considerations can be made on a new experimental setup. In Figure 3.2 a few concepts are outlined. The first is based on the original setup used by Staps and Heuvelmans. Advantages are the simplicity and the fact that a part of the setup already exists. The simple modelling leads to an adequate identification process, since a minimum of parameters has to

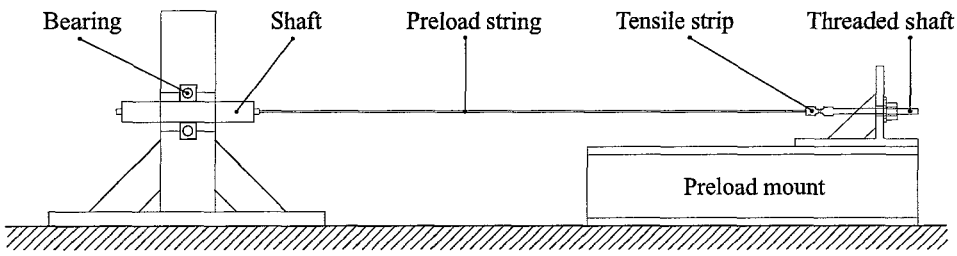

Figure~3.3: Experimental setup

be estimated. However, the existing bearing is rather big, which leads to the requirement of high preloads. A smaller bearing could be content with smaller preloads which are easier to apply.

In the second setup a somewhat realistic approach is created by putting the bearing in a flexible plate. In this case, high preloads cannot be applied as the plate will deform. A Finite Element Method will be needed to model the plate which will handicap the identification process. Besides, the boundary conditions in the experimental setup have to be similar to the ones in the FEM.

The last alternative is based on [7] which describes measurements on a rotating shaft. A disturbance such as the bending vibration of the shaft is suppressed because of its thickness. One bearing can be preloaded with regard to the other bearing, thus no strings are required. However, it is impossible to measure the rotational stiffness of a bearing, for the shaft cannot rotate about its x or y-axis.

The first alternative was chosen because of the simple modelling and the existing setup parts. The second alternative requires an extensive modelling and identification which will complicate the research, while the third alternative cannot yield rotational stiffness results, although this was one of the prominent demands. In Figure 3.3 the setup is sketched to scale. The preloads are applied using a threaded shaft and a long string, which will initiate a negligible amount of stiffness. This stiffness can be calculated through

$$K_{string} = \frac{EA}{l} = 2.46 \cdot 10^5 [N/m] \tag{3.1}$$

which is much smaller than the expected axial stiffness of the bearing, which order of magnitude is $5 \cdot 10^7$ $[N/m]$. Hence, the so called 'dead mass' supported by a relatively slender construction, used by Heuvelmans, is eliminated.

A vibrating string, caused by the excitation, although the effect is hardly noticeable, can effectively be damped by putting pieces of foam around the string. The vibration frequency of the string is dependent on the preload. Therefore, the preload can be measured by determining the vibration frequency, if the vibration length is known and kept constant. Details are available in Appendix B.

During the actual measurements, the preload is measured using a tensile strip, which was already available in the threaded shaft used in [15]. In Figure 3.4 the calibration and measurement of the strain, used for deriving the preload, is shown. Details on the calibration are available in Appendix C.

The complex transfer measurement is done using DIFA, which is schematically drawn in Figure 3.5. The shaft is excited by one or two shakers controlled by DIFA, depending on the

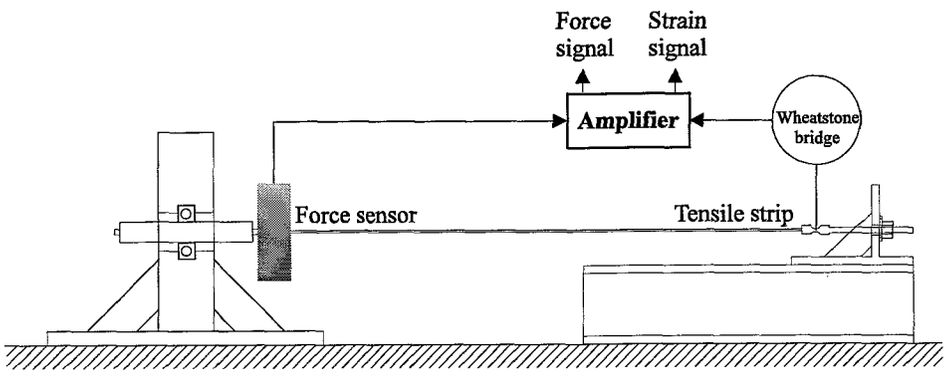

Figure~3.4: The calibration of the tensile strip

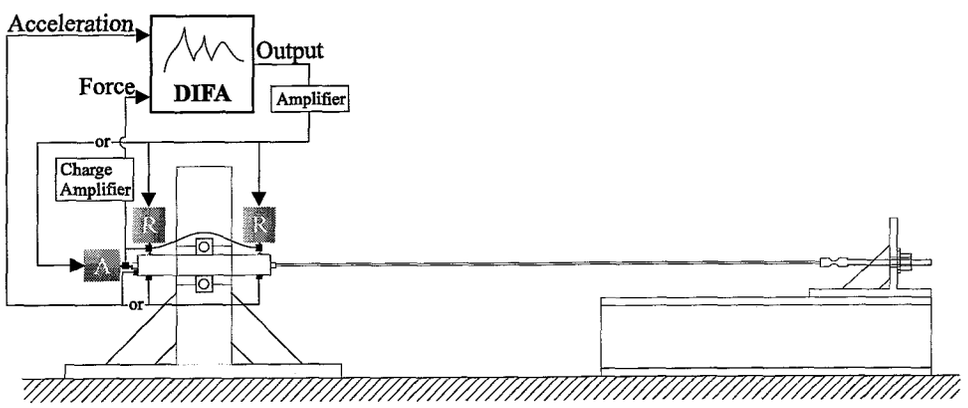

Figure~3.5: The measurement procedure of the transfer function

load situation. Both, the actual applied force and the resulting acceleration are measured and passed to the DIFA system. In a radial excitation only the two shakers marked with 'R', will be used. Likewise, in an axial excitation, only the 'A' marked shaker will be used. After a measurement, the data is converted to Matlab, which is used for calculating the average[1] shaft acceleration and subsequently a particular transfer function component with matching coherence function.

During a measurement using the 'R' marked shakers, the shaft will bend under the excitation load. When the bending stiffness has the same order of magnitude as the bearing stiffness, then precautions have to be taken in the bearing stiffness estimation. In that case, also the estimated mass will differ from the actual shaft mass, because while in bending vibration, the shaft is not in rigid motion. This shaft deformation is sketched in Figure 3.6. The equation of motion for the bending vibration of a shaft according to Bernoulli[2], is

$$\rho A \frac{\partial^2 w(x,t)}{\partial t^2} + EI \frac{\partial^4 w(x,t)}{\partial x^4} = p(x) \tag{3.2}$$

[1]The transfer function components and coherence functions are determined using the average of ten measurements.

[2]Daniel Bernoulli, Professor of applied mathematics, born on Februari 2nd, 1700 in Groningen, died on March 17th, 1782.

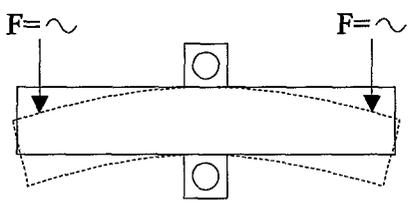

Figure 3.6: Shaft deformation under excitation load

Using separation of variables

$$w(x,t) = y(x)s(t) \tag{3.3}$$

in which $y(x)$ describes the shape of the shaft in the outmost position and $s(t)$ the motion of one material point of the shaft, Equation 3.2 can be transformed to

$$m\ddot{s}(t) + ks(t) = F \tag{3.4}$$

with

$$m_{eq} = \int_{shaft} \rho A y^2(x) dx \tag{3.5}$$

$$k_{shaft} = \int_{shaft} EI \frac{\partial^4 y(x)}{\partial x^4} y(x) dx \tag{3.6}$$

This is equivalent to a single degree of freedom mass-spring system. Hence an equivalent mass and stiffness can be calculated by evaluating Equation 3.5 and 3.6, by assuming

$$y(x) = \cos\left(\frac{\pi x}{l}\right) \tag{3.7}$$

for the first eigenmode, with $l = 0.20$. This yields $m_{eq} = 1.013$ $[kg]$ and $k_{shaft} = 1.176 \cdot 10^8$ $[N/m]$, which indicates that the effective mass is less than the actual shaft mass and that the bending stiffness of the shaft has the same order of magnitude as the bearing stiffness. The bending stiffness of the shaft can also be calculated statically, using the standard equation for a bending situation as sketched in Figure 3.7.

$$w = \frac{Fl^3}{48EI}$$

or

$$F = \frac{48EI}{l^3} w = k_{stat} w$$

Hence, $k_{stat} = 1.159 \cdot 10^8$ $[N/m]$, which justifies the dynamic result. In the actual measurements the shaft will be excited at a certain distance from both ends. These rigid vibrating ends are not taken into account in the calculation of the mass. Therefore, the shaft mass as calculated in Equation 3.5 must be completed with this extra mass. Eventually, the estimated effective mass is 1.3 $[kg]$.

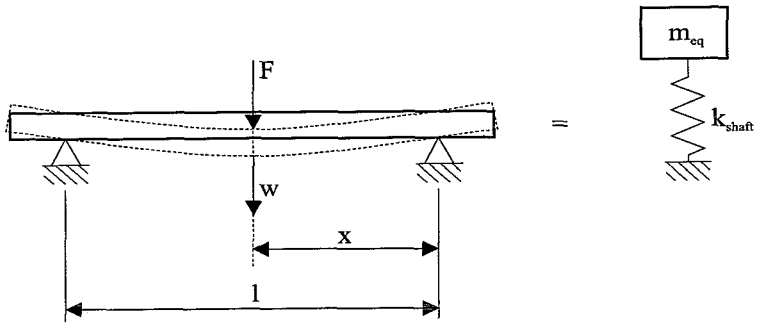

Figure 3.7: Equivalent expressions for a bending beam

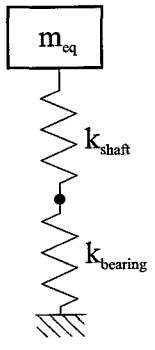

Figure 3.8: Combined stiffness of the shaft and the bearing

In case of an angular contact bearing, the force will not affect the shaft in the middle because of the contact angle. As a result of the shifted force vector, the shaft will bend according to

$$F = \frac{48EI}{3l^2x - 4x^3}w = k_{stat}w$$

Therefore, in case of an angular contact bearing, $k_{shaft} = 1.2902 \cdot 10^8$ $[N/m]$.

In practice however, the motion of the shaft is determined by both the bending stiffness and the bearing stiffness. This situation is simplified in Figure 3.8. In the actual measurements the *combined stiffness* will be measured, which will equal

$$K_{tot} = \frac{1}{\frac{1}{K_{shaft}} + \frac{1}{K_{bearing}}} \tag{3.8}$$

when measured in radial direction. Therefore, after the measurements and data fits the actual radial bearing stiffness needs to be calculated using Equation 3.8. In the case of rotational stiffnesses, this effect can be neglected, since the rotational stiffness of the bearing is much smaller than the bending stiffness of the shaft. Obviously, in the axial direction no bending occurs.

Chapter 4

The Identification Process

In this chapter a brief outline will be given of the used identification algorithms. The Least Squares and Instrumental Variables Method were investigated and augmented with weighting factors in [2]. The third method, Amplitude Fitting [6], will be discussed and subsequently used for deriving new weighting factors, which will unjustify the previous factors used in [2].

4.1 Identification Algorithms

In Appendix D, the Least Squares and Instrumental Variables identification algorithms are outlined in brief. These algorithms are capable of performing multiple-degree-of-freedom (MDOF) fits on mechanical systems like

$$\underline{M}\ddot{q} + \underline{B}\dot{q} + \underline{K}q = f \tag{4.1}$$

The Least Squares algorithm minimizes the fit error by solving

$$\underline{A}^T \underline{A} \hat{\underline{X}}_{ls} = \underline{A}^T \underline{E} \tag{4.2}$$

in which $\underline{A}$ and $\underline{E}$ contain the model characteristics and the experimental data. $\hat{\underline{X}}_{ls}$ contains the unknown parameters of Equation 4.1. The Instrumental Variables algorithm minimizes the difference between the measurements and the model by solving

$$\underline{V}^T \underline{A} \hat{\underline{X}}_{iv} = \underline{V}^T \underline{E} \tag{4.3}$$

iteratively. The matrix $\underline{V}$ contains the so-called instrumental variables output which can be considered as an estimate of the noise-free system.

4.2 Amplitude Fitting

Amplitude fitting [6] is appropriate if the amplitude of a measured transfer function is more accurate than the phase. Unlike the Least Squares and Instrumental Variables method, this is a single-degree-of-freedom fit procedure. A well separated peak in the transfer function can be approximated by a single mode response of

$$\ddot{y} + 2\Omega_k \xi_k \dot{y} + \Omega_k^2 y = P_k e^{j\omega t} \tag{4.4}$$

in which Ω_k and ξ_k are the structural frequency and damping for the particular mode k. P_k is the participation factor for the mode and is obviously equal to the reciprocal of the modal mass. At a given frequency ω_i, the steady state amplitude of the response is given by

$$A_i = \frac{P_k}{\sqrt{\left(\Omega_k^2 - \omega_i^2\right)^2 + \left(2\Omega_k \xi_k \omega_i\right)^2}} = \frac{P_k}{D_i} \tag{4.5}$$

which can be written as

$$A_i D_i - P_k = 0 \tag{4.6}$$

Scaling of Equation 4.6 with the amplitude A_i results in

$$A_i^2 D_i - A_i P_k = 0 \tag{4.7}$$

Solving Equation 4.7 by means of least squares will lead to a considerably more accurate result than solving Equation 4.6 in a similar way.

Equation 4.5 cannot be exact due to errors in the experimental data, therefore it may be written as

$$A_i + \varepsilon_i = \frac{P_k}{D_i} \tag{4.8}$$

or

$$A_i D_i - P_k = -\varepsilon_i D_i \tag{4.9}$$

which indicates that the minimized error is $\sum_{i=1}^{n} \left(\varepsilon_i D_i\right)^2$, using least squares. Conspicuous is the 'weighting factor' D_i, which is minimum at resonance. This means that sample points near resonance are given a lower weighting factor than those away from the peak. This is usually undesirable since points farther away from the peak are contaminated by residues from adjacent modes and suffer from a worse signal-noise ratio than points in the peak.

Equation 4.7 with errors can be written as

$$\left(A_i + \varepsilon_i\right)^2 = \left(A_i + \varepsilon_i\right) \frac{P_k}{D_i} \tag{4.10}$$

or

$$\left(A_i^2 + 2\varepsilon_i A_i + \varepsilon_i^2\right) D_i = A_i P_k + \varepsilon_i P_k \tag{4.11}$$

Simplifying Equation 4.11 using Equation 4.8 and neglecting the second order error terms, yields

$$A_i^2 D_i - A_i P_k = -\varepsilon_i P_k \tag{4.12}$$

which shows that, when the problem is scaled, the minimized error is $\sum_{i=1}^{n} \left(\varepsilon_i\right)^2$, since P_k is a constant.

4.3 Weighting Factors

A similar operating procedure can be applied on the Least Squares and Instrumental Variables method. Like in the previous section the measured transfer can be divided into a theoretical and a noisy part.

$$\underline{H_e}(\omega_i) = \underline{H_t}(\omega_i) + \underline{\varepsilon}(\omega_i) \tag{4.13}$$

Therefore, Equation D.7 can be written as

$$\underline{Z_t}(\omega_i)\left(\underline{H_e}(\omega_i) - \underline{\varepsilon}(\omega_i)\right) - \underline{I} = \underline{0} \tag{4.14}$$

Then, the error (Equation D.8) is

$$\underline{S_i} = \underline{Z_t}(\omega_i)\underline{H_e}(\omega_i) - \underline{I} = \underline{Z_t}(\omega_i)\underline{\varepsilon}(\omega_i) \tag{4.15}$$

which demonstrates that in the Least Squares method, the minimized error is

$$\sum_{i=1}^{n} \left(\underline{Z_t}(\omega_i)\underline{\varepsilon}(\omega_i)\right)^T \left(\underline{Z_t}(\omega_i)\underline{\varepsilon}(\omega_i)\right) \tag{4.16}$$

Like in the unscaled amplitude fit, the minimized error contains a *weighting factor* which is minimum at resonance, which, in this case, is $\underline{Z_t}(\omega_i)$. Now, the same argumentation as used in the previous section can be used to scale Equation D.8 with the experimental transfer $\underline{H_e}(\omega_i)$ or the Instrumental Variables output $\underline{H_a}(\omega_i)$. The weighting factors used in [2] underlie a complete other argumentation, in which the peaks are weighed low and the 'valleys' weighed high, which is, according to this theory, incorrect.

4.4 Numerical Evaluation

On behalf of the numerical evaluation of the identification processes, a three degree of freedom mass-spring-damper model is used, which will be contaminated with several amounts of normally distributed noise. Since the Amplitude Fit procedure is only suitable for SDOF estimations, only the Least Squares and Instrumental Variables algorithms are considered here. The system, depicted in Figure 4.1, can be described, using

$$\underline{M}\ddot{q} + \underline{B}\dot{q} + \underline{K}q = F \tag{4.17}$$

with $k = 1\ [N/m]$, $b = 0.1\ [Ns/m]$, $m_1 = 1\ [kg]$, $m_2 = 2\ [kg]$ and $m_3 = 3\ [kg]$ resulting in

$$\underline{M} = \begin{bmatrix} 1 & & \\ & 2 & \\ & & 3 \end{bmatrix} \tag{4.18}$$

$$\underline{B} = \begin{bmatrix} 0.2 & -0.1 & \\ -0.1 & 0.2 & -0.1 \\ & -0.1 & 0.2 \end{bmatrix} \tag{4.19}$$

$$\underline{K} = \begin{bmatrix} 2 & -1 & \\ -1 & 2 & -1 \\ & -1 & 2 \end{bmatrix} \tag{4.20}$$

The amount of noise can be defined as

$$\eta = \frac{\sigma_{noise}}{\max\left(|H|\right)} \cdot 100\% \tag{4.21}$$

in which σ_{noise} is the standard deviation of the normal distributed noise component and $\max\left(|H|\right)$ is the maximum of the undisturbed transfer function. The used noise levels are printed in Table 4.1. The estimation errors are calculated by adding all least squares errors:

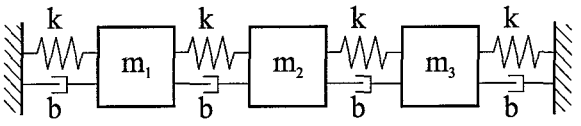

Figure 4.1: A three-degree-of-freedom mass-spring-damper system

Level	η [%]
1	1.1
2	2.1
3	3.2
4	4.3

Table 4.1: Noise levels

$$\varepsilon = \sum_i \sum_j \left(X - \hat{X}\right)^T \left(X - \hat{X}\right) \tag{4.22}$$

The mass matrix is assumed to be known and the stiffness and damping matrix are assumed to be symmetrical. The identification results are shown in tables 4.2 and 4.3.

The identification process is repeated 100 times. Then, the mean fit results are calculated as well as the mean error and the variance of the error. Adding more noise obviously increases the estimation error as well as the variance. The Instrumental Variables procedure always yields smaller error values but the effect is stronger in case of higher noise amounts. However, the used procedure fails when much higher noise amounts are used, since, in that case, the Instrumental Variables initial estimate (i.e. the Least Squares estimate) is useless.

The used programs are printed in Appendix F. The application of weighting factors appeared not to be useful in the Least Squares and Instrumental Variables method, for the total estimation error could not be systematically decreased. Besides, in a single-degree-of-freedom environment, the concept of weighing is easy to understand, unlike in a multiple-degree-of-freedom environment where the use of a filled weighting matrix is indistinct.

Noise level	$\hat{B}$	$\hat{K}$	Mean error	Variance
1	$\begin{bmatrix} 0.19 & -0.09 & -0.01 \\ & 0.18 & -0.09 \\ & & 0.19 \end{bmatrix}$	$\begin{bmatrix} 1.99 & -0.98 & -0.02 \\ & 2.03 & -1.04 \\ & & 2.08 \end{bmatrix}$	$2.78 \cdot 10^{-2}$	$1.81 \cdot 10^{-4}$
2	$\begin{bmatrix} 0.16 & -0.07 & -0.01 \\ & 0.14 & -0.06 \\ & & 0.15 \end{bmatrix}$	$\begin{bmatrix} 1.97 & -0.93 & -0.07 \\ & 2.10 & -1.13 \\ & & 2.31 \end{bmatrix}$	$2.45 \cdot 10^{-1}$	$1.15 \cdot 10^{-2}$
3	$\begin{bmatrix} 0.14 & -0.05 & -0.01 \\ & 0.10 & -0.03 \\ & & 0.12 \end{bmatrix}$	$\begin{bmatrix} 1.92 & -0.86 & -0.12 \\ & 2.20 & -1.24 \\ & & 2.59 \end{bmatrix}$	$7.58 \cdot 10^{-1}$	$1.14 \cdot 10^{-1}$
4	$\begin{bmatrix} 0.12 & -0.03 & -0.02 \\ & 0.07 & -0.02 \\ & & 0.08 \end{bmatrix}$	$\begin{bmatrix} 1.96 & -0.79 & -0.21 \\ & 2.27 & -1.30 \\ & & 2.86 \end{bmatrix}$	$1.48 \cdot 10^{0}$	$3.40 \cdot 10^{-1}$

Table 4.2: Least Squares identification

Noise level	$\hat{B}$	$\hat{K}$	Mean error	Variance
1	$\begin{bmatrix} 0.20 & -0.10 & 0.00 \\ & 0.20 & -0.10 \\ & & 0.21 \end{bmatrix}$	$\begin{bmatrix} 2.00 & -1.00 & 0.00 \\ & 2.00 & -1.00 \\ & & 2.00 \end{bmatrix}$	$1.47 \cdot 10^{-2}$	$7.54 \cdot 10^{-5}$
2	$\begin{bmatrix} 0.21 & -0.10 & 0.00 \\ & 0.21 & -0.10 \\ & & 0.19 \end{bmatrix}$	$\begin{bmatrix} 2.02 & -1.01 & 0.00 \\ & 2.01 & -1.00 \\ & & 2.00 \end{bmatrix}$	$5.96 \cdot 10^{-2}$	$1.48 \cdot 10^{-3}$
3	$\begin{bmatrix} 0.21 & -0.11 & 0.01 \\ & 0.22 & -0.12 \\ & & 0.24 \end{bmatrix}$	$\begin{bmatrix} 2.02 & -1.03 & 0.01 \\ & 2.02 & -1.00 \\ & & 2.00 \end{bmatrix}$	$1.56 \cdot 10^{-1}$	$1.08 \cdot 10^{-2}$
4	$\begin{bmatrix} 0.25 & -0.09 & -0.03 \\ & 0.21 & -0.11 \\ & & 0.21 \end{bmatrix}$	$\begin{bmatrix} 2.05 & -1.02 & 0.00 \\ & 2.02 & -1.01 \\ & & 2.02 \end{bmatrix}$	$2.06 \cdot 10^{-1}$	$1.02 \cdot 10^{-2}$

Table 4.3: Instrumental Variables identification

Chapter 5

Experimental Results

The Matlab function `spectrum` was used to calculate all components of the transfer function. Results are available in Appendix F.3. The attempt to estimate the entire stiffness and damping matrices failed. This is probably caused by the complexity of the total transfer function and the fact that, in some transfer components, the coherence is very bad for some eigenfrequencies. On the matrix diagonal, the coherences are better. Since a multiple-degree-of-freedom (MDOF) fit could not lead to any result, several peaks have to be estimated separately using a single-degree-of-freedom (SDOF) procedure, for which the basic theory remains the same. The results of a SDOF fit however, cannot be compared to elements of the theoretical stiffness matrix without 'conversion'. Therefore, these results will be compared to the corresponding SDOF fit on the theoretical transfer function. For the actual SDOF fits, the Instrumental Variables procedure is used.

5.1 SDOF Stiffness and Damping Results

In case of a purely axial preload the radial stiffnesses in x and y-direction are equal, since changing the position of the rolling elements appeared to be a negligible effect in the resulting stiffness. This also applies to the rotational stiffnesses about the x and y-axis. Therefore, in theory, only three eigenfrequencies evolve. The stiffness and damping results for the deep groove ball bearing NSK 6802 are printed in Figure 5.2, 5.3 and 5.4.

The theoretical model shows the same trends as the experimental results but seems to need a multiplication to match with the experimental data, which could indicate an incorrect stiffness parameter K_n. The modelled stiffnesses are all smaller than the experimental data, but a multiplication factor would not be equal in all directions.

Using the SDOF procedure, only the diagonal components can be studied. The so-called *coupling terms* can only be analyzed visually by comparing the measured and theoretical transfer functions, which are printed in Appendix F.3. Real similarities are hard to see and effects such as shaft flexibility in the radial direction cannot be traced. The symmetry of the model and the experiments is discussed in the topic on reciprocity.

The main goal of this research is focussed on the bearing stiffness rather than bearing damping. However, the measured transfer functions yield both stiffness and damping values. Therefore, also the damping results are presented. In Lim's theory the damping is assumed to be Rayleigh damping, which is proportional to the stiffness. The axial and rotational damping results show an increasing trend, like the Rayleigh case. However, the radial damping results

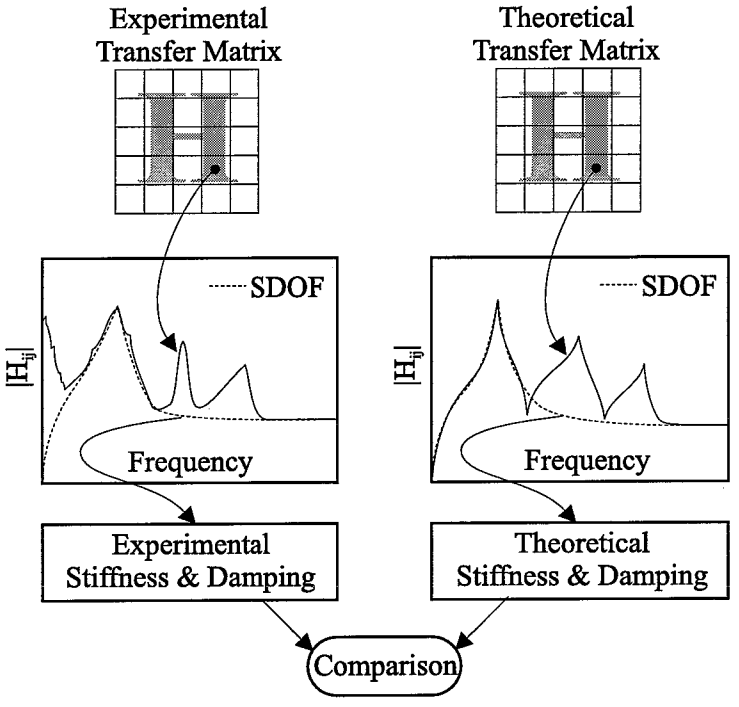

Figure 5.1: Comparison of the experimental SDOF fit with the theoretical SDOF fit

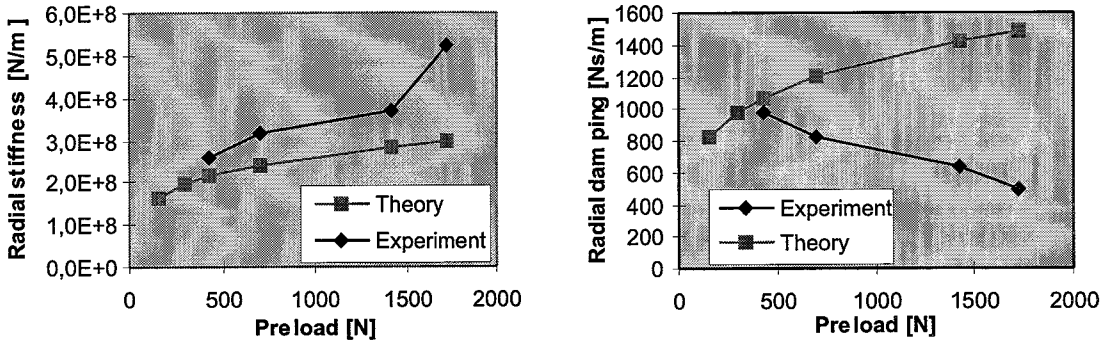

Figure 5.2: Left: The measured and theoretical *radial* stiffness. Right: The measured *radial* damping compared with the used Rayleigh damping. (Deep groove ball bearing NSK 6208)

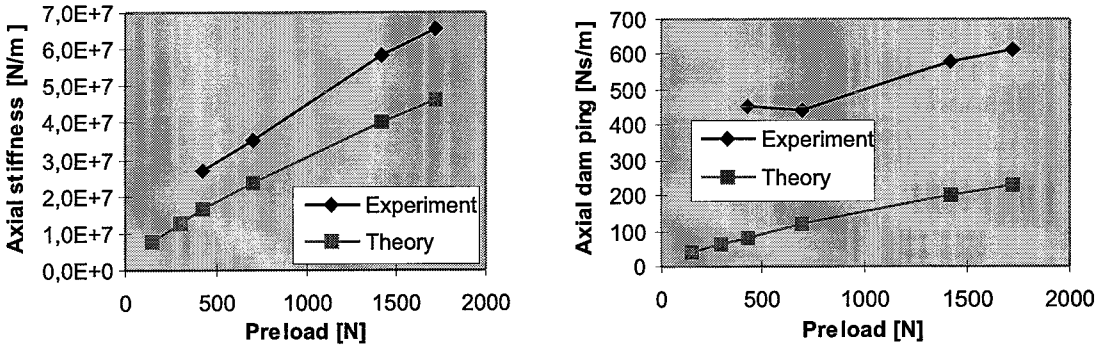

Figure 5.3: Left: The measured and theoretical *axial* stiffness. Right: The measured *axial* damping compared with the used Rayleigh damping. (Deep groove ball bearing NSK 6208)

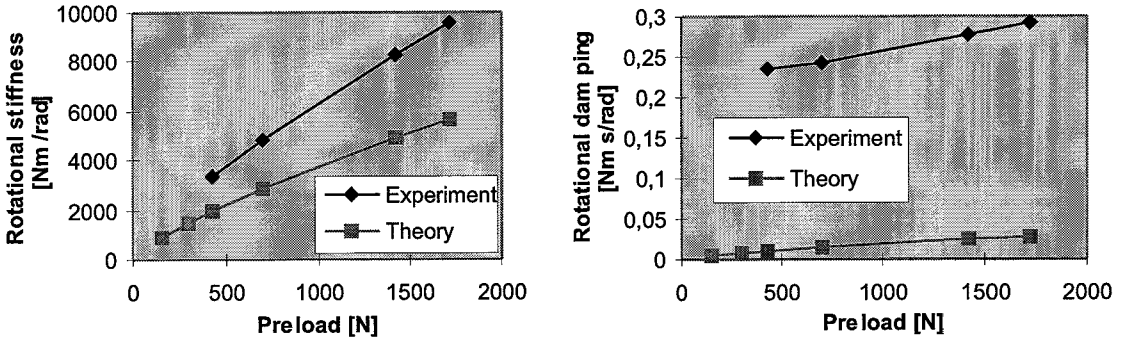

Figure 5.4: Left: The measured and theoretical *rotational* stiffness. Right: The measured *rotational* damping compared with the used Rayleigh damping. (Deep groove ball bearing NSK 6208)

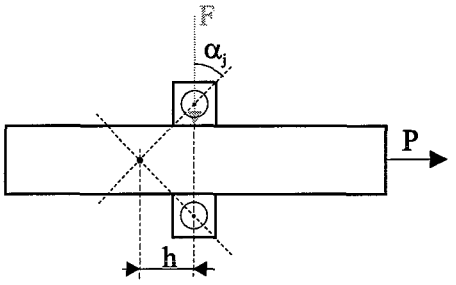

Figure 5.5: The point of rotation in a bearing setup with resulting momentum

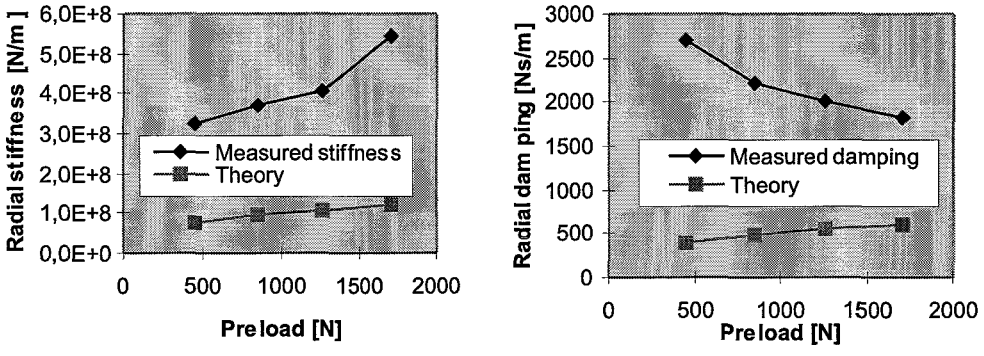

Figure 5.6: Left: The measured and theoretical *radial* stiffness. Right: The measured *radial* damping compared with the used Rayleigh damping. (Angular contact bearing RPF 7208)

show that the damping decreases in case of an increasing preload. Therefore, the assumption to use Rayleigh damping is not justified. In [9] several damping models are discussed and some experimental radial damping results are presented. These results show a decrease in the radial damping when applying higher preloads, as well, in case of a non-rotating shaft. The results in [9] also show that the damping differs when the shaft rotates at a particular speed. At certain speeds, the damping will be determined by elasto-hydrodynamic lubrication which is a combination of elastic deformation of the bearing elements and a supportive effect of the oil film, which will complicate the damping prediction.

In the case of a deep groove ball bearing, the effect of the loaded contact angle is very small, since the rotation point is approximately in the centre of the bearing (Figure 5.5). For example, the application of a radial excitation in y-direction should lead to a small rotation about the x-axis, because the tiny loaded contact angle yields a small momentum about the x-axis. For better insight, measurements were carried out on an angular contact bearing, since these bearings exhibit a greater contact angle.

Like in the deep groove ball bearing case, all modelled stiffnesses are smaller than the experimentally determined data. The stiffness trends however, are described well. The difference can be caused by the fact that the bearing behaviour is not well separated from the actual measured data or by the difference between the statical nature of the model and the dynamical nature of the measurements. Statical bearing stiffness measurements can give

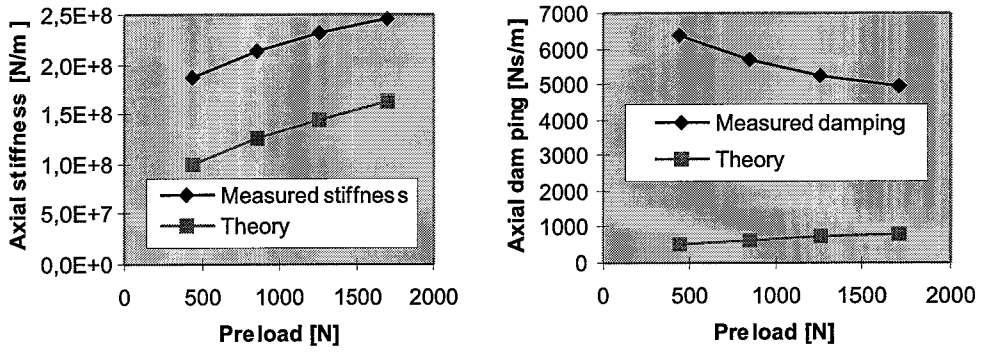

Figure~5.7: Left: The measured and theoretical *axial* stiffness. Right: The measured *axial* damping compared with the used Rayleigh damping. (Angular contact bearing RPF 7208)

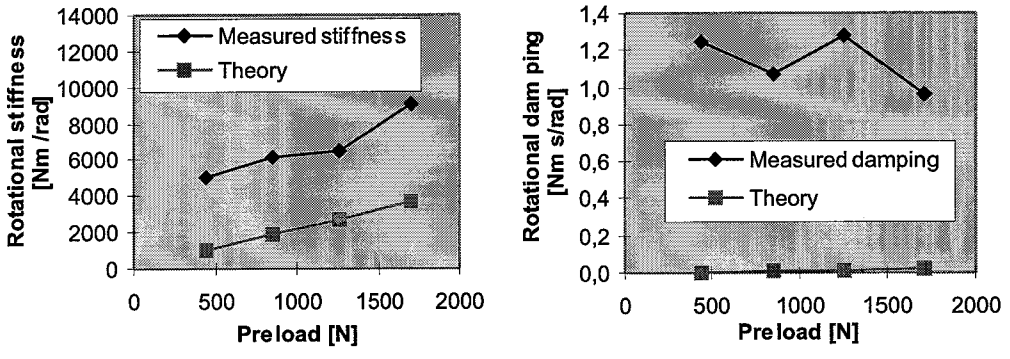

Figure~5.8: Left: The measured and theoretical *rotational* stiffness. Right: The measured *rotational* damping compared with the used Rayleigh damping. (Angular contact bearing RPF 7208)

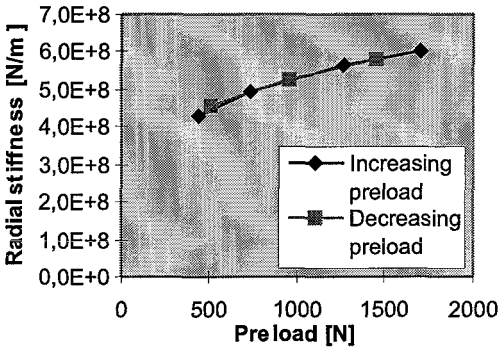

Figure 5.9: Measured radial stiffness, during increasing and decreasing preload. (Deep groove ball bearing NSK 6208)

clarification on this matter.

Unlike in the deep groove ball bearing case, the measured angular contact damping values all decrease with increasing preloads. Apparently, the contact angle of a bearing influences the amount of damping.

Because of the contact angle, one could expect a smaller radial stiffness and a higher axial stiffness in the angular contact bearing case, like in Figure 2.4. However, in general, an angular contact bearing has more rolling elements than an equally sized deep groove ball bearing. Therefore, the radial stiffness of the angular contact bearing is not significantly smaller. The axial stiffness is higher because of both the contact angle and the higher number of rolling elements.

5.2 Hysteresis and Reproducibility

Applying a higher axial preload and subsequently releasing the preload, shows the effect of hysteresis in a bearing. This is shown in Figure 5.9. Apparently, there is no hysteresis.

The repeatedly performing of the measurements proved that the experimental setup is capable of producing the same results under the same circumstances later on. However, the hysteresis experiment stiffnesses, printed in Figure 5.10 together with the previous acquired radial stiffness results, are higher than the previous measured results. In the period between the hysteresis measurements and the actual stiffness measurements, a constant preload was applied on the bearing, which always kept the same position. From the figure the supposition can be drawn that the rolling elements are 'pulled through' the oil film or damaged under the high preload, especially because of the last experimental stiffness, which seems to be out of proportion. Performing the same measurements after creating a new oil film by rotating the shaft manually or putting the bearing in another position yielded the same stiffness values as obtained in the hysteresis experiment. Therefore, the influence of time has yet to be investigated.

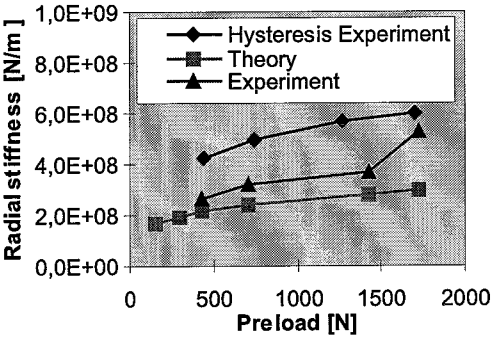

Figure~5.10: Hysteresis results compared with previous radial stiffness results

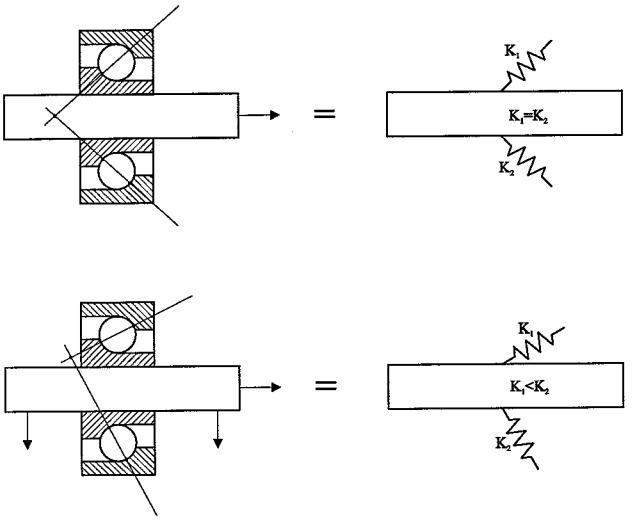

Figure~5.11: The influence of radial preloads

5.3 Coupling Terms and Reciprocity

Using a purely axial preload will cause the coupling terms concerning the axial motion to be zero. This is clarified in Figure 5.11. An excitation in the axial direction will cause the shaft to move only in the axial direction, because all rolling elements have the same contact angle and identical stiffnesses. Applying radial preloads as well, causes the contact angles to change and to load some rolling elements more than others, resulting in higher stiffnesses in the concerning elements. Hence, the situation is no longer symmetrical and an excitation will as well cause the shaft to move in other directions, related to the preloads. In this research, the preload was meant to be purely axial, but the weight of the shaft yields a tiny radial preload in the y-direction. This preload cannot be neglected since the effect is rather strong. The theoretical stiffness matrices and therefore the theoretical transfer functions still have some zero components, unlike the measured transfer functions. The disturbing factors which cause these 'zero terms' to be non-zero are the flexibility of the shaft and the fact that an excitation is not always exactly performed the right direction, which suits with Figure 2.7 and accompanying theory.

The model always yields a symmetric matrix, that is, the model is reciprocal. The experimental matrix should be symmetrical, according to the model. In this consideration, all 'zero terms' in the experimental results will not be considered, since these terms are observed as the result of some experimental imperfections. In Figure 5.12 the deep groove ball bearing transfer functions $H_{x\theta_y}$, $H_{\theta_y x}$, H_{yz}, H_{zy}, $H_{z\theta_x}$ and $H_{\theta_z z}$ are drawn. $H_{x\theta_y}$ and $H_{\theta_y x}$ show a great resemblance. The other terms however have less similarity, which could be explained by the fact that the responsible radial preload, i.e. the proper weight of the shaft, is low. In the low preload region, the stiffness matrix terms are not well determined, like mentioned in Chapter 2. Besides, the radial excitation load is in the same order of magnitude as this radial preload. The comparison for an angular contact bearing appeared to be unfeasible since the frequency scale of $H_{\theta_y x}$ is not sufficient, because smaller frequency steps were needed in the rotational measurements. Nevertheless, the symmetry of the model seems to be supported by the experiments.

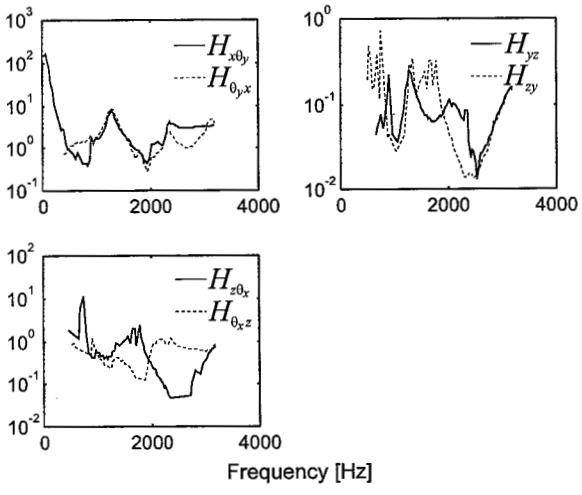

Figure 5.12: Verification of the transfer matrix symmetry. (Deep groove ball bearing NSK 6208, axial preload = 427 $[N]$)

Chapter 6

Conclusions and Recommendations

6.1 Conclusions

- Combined preloads result in non-monotonously increasing or decreasing stiffness matrix terms.
- Tiny preloads or excitation disturbances cause some matrix coupling terms to increase enormously, whereas they would be zero.
- The experimental setup is capable of providing reproducible measurements with acceptable coherence, especially on the main diagonal of the transfer matrix. However, the stiffness values from the hysteresis experiment appeared to be higher than the actual stiffnesses. This is probably caused by the long period of axial preload on the bearing.
- In the actual experiments a well directed excitation is hard to establish, resulting in non-zero transfer matrix terms which should be zero.
- The concept of weighing, according to the amplitude fit algorithm, in a multiple-degree-of-freedom identification algorithm was not able to systematically reduce estimation errors.
- The estimation of an entire stiffness matrix appeared to be unfeasible. Apparently, the measured transfer function differed too much from a theoretical model for proper identification results. Therefore single-degree-of-freedom fits were used to estimate direct stiffnesses, i.e. fits on the diagonal components of the transfer function.
- Single-degree-of-freedom fits cannot be applied on the transfer coupling terms, hence they have to be compared visually to the model.
- Hysteresis in the bearing stiffness could not be found.
- All experimental stiffnesses are higher than the accompanying theoretical stiffnesses. However, the model is able to describe the stiffness trends. Hence, if the bearing behaviour is well separated from the experimental data, the model is only suitable for qualitative predictions in stead of quantitative predictions. Another possibility is the difference between the dynamical nature of measurements and the statical nature of the model. For certainty, statical measurement could be performed on the bearings.

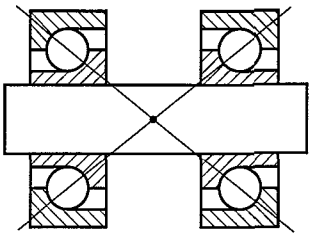

Figure 6.1: Proposal for a new experimental setup

- The bearing damping cannot be described using Rayleigh damping, which is proportional to the stiffness. On the contrary, the radial bearing damping tends to decrease for increasing axial preload in the deep groove ball bearing case. In the angular contact bearing case *all* damping values decrease for increasing axial preload.
- The experiments seem to support the model's symmetry.

6.2 Recommendations

- The shaft construction is not recommendable for future measurements. The shaft in this construction bends under a radial excitation which influences all radial related transfer matrix terms. Besides, the use of two radial shakers will hamper the rotation about the radial excitation axis. Therefore, another construction has to be developed, e.g. like shown in Figure 6.1.
- Experiments with combined preloads have yet to be performed.
- Statical measurements on the bearing can give clearness on the difference aspects on dynamical and statical measurements and eventually could justify the bearing model quantitatively.
- Measurements on a rotating shaft are more realistic.
- The effect of time on the bearing stiffness has yet to be investigated, especially in high-preload cases without shaft rotation. This is probably related to the lubrication matter.
- Research on lubrication and damping matters are an obvious next step in this project, since damping can decrease noise radiation.

Appendix A

Experimental Setup Parts

In this Appendix, some characteristics of the experimental setup including measurement tools are printed.[1]

String

Young's modulus	$E = 1.75 \cdot 10^{11}\ [N/m^2]$
Poisson's modulus	$\mu = 0.33\ [-]$
Diameter	$D = 1.6\ [mm]$
Length	$l = 1.43\ [m]$
Density	$\rho = 7100\ [kg/m^3]$
Axial stiffness	$k = \frac{EA}{l} = 2.46 \cdot 10^5\ [N/m]$
Longitudinal wave speed	$c_L = \sqrt{\frac{E}{\rho}\frac{1-\mu}{(1+\mu)(1-2\mu)}} = 6043\ [m/s]$
Transversal wave speed	$c_T = \sqrt{\frac{E}{\rho}\frac{1}{2(1+\mu)}} = 3044\ [m/s]$
Longitudinal eigenfrequency	$f_L = \frac{c_L}{\lambda} = 2113\ [Hz]$
Transversal eigenfrequency	$f_T = \frac{c_T}{\lambda} = 1064\ [Hz]$

Shaft

Young's modulus	$E = 2.1 \cdot 10^{11}\ [N/m^2]$
Poisson's modulus	$\mu = 0.33\ [-]$
Length	$l = 0.26\ [m]$
Density	$\rho = 7850\ [kg/m^3]$
Mass	$m = 2.45\ [kg]$
Radial inertia	$J_x = J_y = 1.24 \cdot 10^{-2}\ [kg/m^2]$
Axial inertia	$J_z = 6.88 \cdot 10^{-4}\ [kg/m^2]$
Longitudinal eigenfrequency	$f_L = 11990\ [Hz]$
Transversal eigenfrequency	$f_T = 5999\ [Hz]$

[1] Details can be found in [2].

Measurement tools

Amplifier	HBM AE 3407A
Force sensor	Automation Industries TD 0500 S/N 700
Tensile strip	TUE
Acceleration sensor	PCB 303A02 S/N 18443
Acceleration sensor	PCB 303A02 S/N 18444
Acceleration sensor	PCB 303A03 S/N 20353
Force sensor	Kistler 9301A S/N 13229
Force sensor	Kistler 9301A S/N 150391
Charge amplifier	Kistler 5007 S/N 200732
Charge amplifier	Kistler 5007 S/N 52900
Signal amplifier	LDS TPO25
Shaker	LDS V201
Shaker	LDS V201
DIFA (Hardware)	Dynamic Signal Analyzer 220-12 S/N 93952106
DIFA (Software)	DIFA D_TAC200 Version 3.31D

NSK 6208 Deep Groove Ball Bearing

Number of rolling elements	$z = 9$
Rolling element load-deflection stiffness constant	$K_n = 1.10 \cdot 10^{10}$
Unloaded groove curvature centres distance	$A_0 = 5.953 \cdot 10^{-4}$ $[m]$
Unload contact angle	$\alpha_0 = 0^o$
Radial distance to inner raceway groove curvature centre	$r_j = 3.01488 \cdot 10^{-2}$ $[m]$

RPF 7208 BE Angular Contact Bearing

Number of rolling elements	$z = 12$
Rolling element load-deflection stiffness constant	$K_n = 6.262 \cdot 10^9$
Unloaded groove curvature centres distance	$A_0 = 5.571 \cdot 10^{-4}$ $[m]$
Unload contact angle	$\alpha_0 = 40^o$
Radial distance to inner raceway groove curvature centre	$r_j = 3.012 \cdot 10^{-2}$ $[m]$

Appendix B

Alternative Preload Measurement

The equation of motion for the vibrating string of Figure B.1 is

$$P\frac{\partial^2 w(x,t)}{\partial x^2} = \rho_l \frac{\partial^2 w(x,t)}{\partial t^2} \tag{B.1}$$

or

$$c^2\frac{\partial^2 w(x,t)}{\partial x^2} = \frac{\partial^2 w(x,t)}{\partial t^2} \tag{B.2}$$

with

$$c = \sqrt{\frac{P}{\rho_l}} \tag{B.3}$$

where ρ_l is the density per unit length of the string. The vibration frequencies are

$$f_n = \frac{nc\pi}{2\pi l} = \frac{nc}{2l} \tag{B.4}$$

Therefore the relationship between the preload P and the fundamental frequency, i.e. $n = 1$, is

$$P = \rho A\,(2lf)^2 \tag{B.5}$$

using $\rho_l = \rho A$, in which ρ is the density of the string and A the cross sectional area (see Appendix A). The experimental results are plotted in Figure B.2.

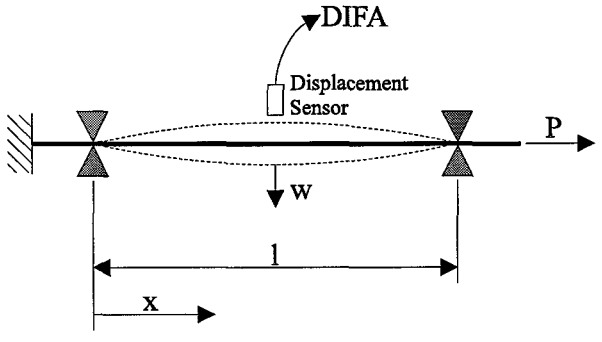

Figure B.1: Alternative preload measurement using a vibrating string

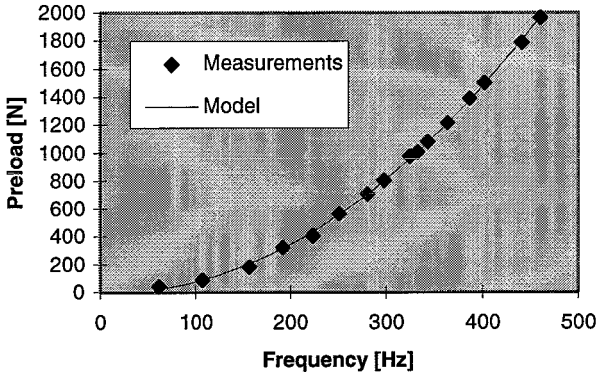

Figure~B.2: Frequency measurement and the model

Equation B.5 can be written as

$$P = a \cdot f^2$$

in which a can be obtained by a curve fit. The model in Figure B.2 is calculated using a fit on a second order polynomial without the zero and first order term, resulting in

$$P = 0.009189 \cdot f^2$$

with an R-squared value of $R^2 = 0.9986$.

Appendix C

Calibration of the Tensile Strip

In Figure C.1 the calibration curve of the tensile strip is printed in which, for a number of preloads, the resulting signal from the tensile strip are drawn. Subsequently, a straight line is fitted through the data points. The equation of the fitted line is

$$F = 207.9 \cdot S + 0.0092 \tag{C.1}$$

with an R-squared value of $R^2 = 0.9985$ which indicates that the measured strain values are very well linearly dependent on the imposed preload. The fitted offset term is negligible with respect to the proportional term.

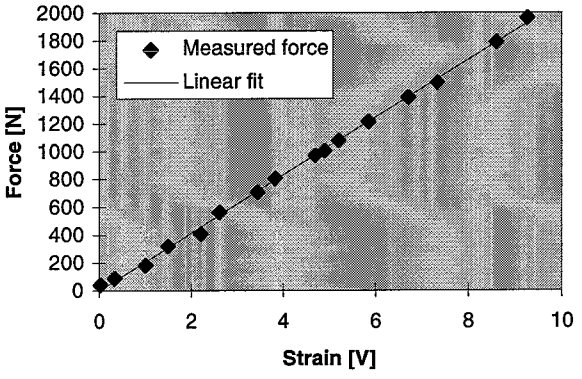

Figure~C.1: The calibration curve which transforms the measured strain signal in the tensile strip (in Volt) into the applied preload (in Newton)

Appendix D

Identification Methods

In this appendix, the Least Squares and Instrumental Variables identification are outlined.

D.1 Least Squares Identification

The motion of a mechanical system can be described with

$$\underline{M}\ddot{q} + \underline{B}\dot{q} + \underline{K}q = f \tag{D.1}$$

In this equation the mass matrix $\underline{M}$, damping matrix $\underline{B}$ and stiffness matrix $\underline{K}$ have to be estimated. Using harmonic excitation

$$f = \hat{f}e^{j\omega t} \tag{D.2}$$
$$q = \hat{q}e^{j\omega t} \tag{D.3}$$

Equation D.1 can be written as

$$\left(-\omega^2\underline{M} + j\omega\underline{B} + \underline{K}\right)\hat{q} = \hat{f} \tag{D.4}$$

or

$$\underline{Z_t}(\omega)\hat{q} = \hat{f} \tag{D.5}$$

in which $\underline{Z_t}$ is the dynamic stiffness. The transfer function matrix $\underline{H_t}(\omega)$ is defined as

$$\hat{q} = \underline{H_t}(\omega)\hat{f} \tag{D.6}$$

Therefore, in theory

$$\underline{Z_t}(\omega)\underline{H_t}(\omega) = \underline{I} \tag{D.7}$$

Now, the theoretical model, represented by $\underline{Z_t}(\omega)$, has to be matched with the experimental transfer matrix $\underline{H_e}(\omega_i)$. The symbol i indicates the sample number. Therefore, $i = 1 \ldots n$ for n samples in one measurement. Clearly, in general $\underline{Z_t}(\omega_i)\underline{H_e}(\omega_i) \neq \underline{I}$. The error to be minimized is

$$\underline{S_i} = \underline{Z_t}(\omega_i)\underline{H_e}(\omega_i) - \underline{I} \tag{D.8}$$

By writing Equation D.8 as

$$\underline{S_i} = \underline{A_i}\underline{X} - \underline{I} \tag{D.9}$$

with

$$\underline{A_i} = \left\{ -\omega_i^2 \underline{H_e}(\omega_i) \quad j\omega_i \underline{H_e}(\omega_i) \quad \underline{H_e}(\omega_i) \right\} \tag{D.10}$$

$$\underline{X} = \left\{ \begin{array}{c} \underline{M} \\ \underline{B} \\ \underline{K} \end{array} \right\} \tag{D.11}$$

the unknown parameters are isolated. Now, the error in the total measured domain is

$$\underline{S} = \underline{AX} - \underline{E} \tag{D.12}$$

with

$$\underline{S} = \left\{ \begin{array}{c} \underline{S_1} \\ \underline{S_2} \\ \vdots \\ \underline{S_n} \end{array} \right\} \tag{D.13}$$

$$\underline{A} = \left\{ \begin{array}{c} \underline{A_1} \\ \underline{A_2} \\ \vdots \\ \underline{A_n} \end{array} \right\} \tag{D.14}$$

$$\underline{E} = \left\{ \begin{array}{c} \underline{I} \\ \underline{I} \\ \vdots \\ \underline{I} \end{array} \right\} \tag{D.15}$$

The overall error can be minimized by solving *the normal equations* for $\underline{\hat{X}_{ls}}$:

$$\underline{A}^T \underline{A} \underline{\hat{X}_{ls}} = \underline{A}^T \underline{E} \tag{D.16}$$

Here, $\underline{\hat{X}_{ls}}$ contains the Least Squares estimates $\underline{\widehat{M}}$, $\underline{\widehat{B}}$ and $\underline{\widehat{K}}$. A considerable accuracy improvement can be achieved by splitting Equation D.12 into a real and an imaginary part, causing the total matrices $\underline{S}$, $\underline{A}$ and $\underline{E}$ to become twice as long. Other improvements can be achieved by assuming all matrices symmetric and removing $\underline{\widehat{M}}$ from the identification process using an a priori calculated mass estimate.

D.2 Instrumental Variables Identification

When a measured signal contains a relatively great amount of noise, the Least Squares estimates will be intolerably inaccurate. The Instrumental Variables method gets around this problem because of its insensitiveness to noise. A priori, little needs to be known about the statistical properties of the noisy signal. In the Instrumental Variables method Equation D.12 will be premultiplied with an instrumental variables matrix $\underline{V}$.

$$\underline{V}^T \underline{S} = \underline{V}^T \underline{AX} - \underline{V}^T \underline{E} \tag{D.17}$$

This matrix $\underline{V}$ is chosen to be highly correlated with the unobserved *noise-free* process variables, but totally uncorrelated with the various additive noise components that corrupt these

signals. In literature many propositions are made concerning the choice of the matrix $\underline{V}$. Here, Young's [13] proposition will be used. The matrix $\underline{V}$ will be built of the undisturbed system output, however, this output is yet unknown. An auxiliary model, with the same properties as the estimated model, is used to produce an estimated undisturbed system output. The total identification algorithm will be iterative and uses an initial parameter estimate (e.g. Least Squares estimate) because of the auxiliary model. In each iteration step the new parameter estimates can be calculated by solving

$$\underline{V}^T \underline{A} \underline{\widehat{X}}_{iv} = \underline{V}^T \underline{E} \tag{D.18}$$

for $\underline{\widehat{X}}_{iv}$, using the following auxiliary model:

$$\underline{V_i} = \left\{ -\omega^2 \underline{H_a}(\omega_i) \quad j\omega \underline{H_a}(\omega_i) \quad \underline{H_a}(\omega_i) \right\} \tag{D.19}$$

$$\underline{V} = \begin{Bmatrix} \underline{V_1} \\ \underline{V_2} \\ \vdots \\ \underline{V_n} \end{Bmatrix} \tag{D.20}$$

in which $\underline{H_a}(\omega_i)$ can be considered as the estimate of the theoretical transfer function $\underline{H_t}(\omega_i)$. Then, the new parameters are used to build a new instrumental variables matrix using the auxiliary model, which in turn can be used to calculate a new instrumental variable estimate. Like the Least Squares method, the Instrumental Variables method can be improved by splitting up the real and imaginary parts of the error equation. Also, the symmetry of the matrices can be taken into account as well as the known mass matrix $\underline{\widehat{M}}$. Details can be found in [2], [13] and [14].

Appendix E

Matlab Programs

```
function [omega_0, xi, P] = Amplifit(H, omega);

% Function AMPLIFIT calculates the eigenfrequency and damping factor from
% the amplitude of a transfer function.
%
% Input:
% H: Transfer function (complex)
% omega: Frequency scale
%
% Output:
% X: Vector containing the eigenfrequency and damping factor
%
% By R.J.W. Knaapen, 1996

H_abs = abs(H);
[len, dim] = size(H);
n = len/dim;

A = [];
B = [];
for i = 1:n,
  A = [A; H_abs(i)^3 H_abs(i)^3*omega(i)^2 -H_abs(i)];
  B = [B; -H_abs(i)^3*omega(i)^4];
end;

X = inv(A'*A)*A'*B;

omega_0 = X(1)^(1/4);
xi      = sqrt(X(2)/(4*omega_0^2) + 0.5);
P       = sqrt(X(3));
```

```
function C = TransMat(dim);

% Function TransMat calculates a transformation matrix C such that:
%
% X = Cx
%
% with: X = [a11 a12 ... a1dim, a21 a22 ... a2dim, ... adimdim]
%       x = [a11 a12 ... a1dim, a22 a23 ... a2dim, ... adimdim]
%
% Matrix x contains the upper triangle of a symmetric matrix.
%
% By R.J.W. Knaapen, 1996

l = CountSum(dim);          % 1 + 2 + 3 + ... + dim
C = zeros(dim^2,l);
for i = 1:dim,
  for j = 1:dim,
    if j<i,
      p = (j-1)*dim+i-CountSum(j-1);
    else,
      p = (i-1)*dim+j-CountSum(i-1);
    end;
    C((i-1)*dim+j, p) = 1;
  end;
end;
```

```
function [X,A,E, C] = LSquare(H, omega, M);

% Function LSquare fits Stiffness, Damping and matrices on a ...
  measured transfer function..
% Transfer function: ACCELERANCE!
%
% Input:
% H Matrix H contains all transfer functions as a function of omega.
% omega Vector omega contains the frequencies.
% M The known mass matrix
%
% Output:
% X Matrix X contains the stiffness, damping and mass matrices.
% A Least Squares matrix (the system)
% E Least Squares matrix (the vector)
% C Transformation matrix for conversion between symmetric ...
  (efficiently stored) and full matrices.
%
% MASS IS KNOWN!
% ASSUMPTION: K and B ARE SYMMETRIC!
%
% By R.J.W. Knaapen, 1996

[len, dim] = size(H);
n = len/dim;

A = [];
E = [];
I = eye(dim);
%disp(['Counting to ' num2str(n)]);
for i = 1:n,
%  disp(i);
  Hhulp = H( (i-1)*dim+1:i*dim, : );
  Z = zeros(2*dim*dim,dim*dim);
  Y = [];
  for m = 1:dim,
    Z((m-1)*2*dim+1:(m-1)*2*dim+dim,       (m-1)*dim+1:(m-1)*dim+dim) = ...
      1/omega(i)*imag(Hhulp);
    Z((m-1)*2*dim+dim+1:(m-1)*2*dim+2*dim, (m-1)*dim+1:(m-1)*dim+dim) = ...
     -1/omega(i)*real(Hhulp);
    Z((m-1)*2*dim+1:(m-1)*2*dim+dim,       dim^2+(m-1)*dim+1:dim^2+(m-1)*dim+dim) = ...
     -1/omega(i)^2*real(Hhulp);
    Z((m-1)*2*dim+dim+1:(m-1)*2*dim+2*dim, dim^2+(m-1)*dim+1:dim^2+(m-1)*dim+dim) = ...
     -1/omega(i)^2*imag(Hhulp);
    Y = [Y; I(:,m)-real(Hhulp)*M(:,m); -imag(Hhulp)*M(:,m)];
  end;
  A = [A; Z];
```

```
  E = [E; Y];
end;

% Construction of the transformation matrix:
%disp('Building transformation matrix');
C_k = TransMat(dim);
C = [C_k, zeros(dim^2, CountSum(dim)); zeros(dim^2, CountSum(dim)), C_k];

% Calculation of the Least Squares Approximation
%disp('Calculating Least Squares Approximation');
A = A*C;
X = inv(A.'*A)*A.'*E;
```

```
function [X, Xleast, Hh] = IVar(H, omega, M);

% Function IVar calculates damping and stiffness matrices from the
% transfer matrix H using the Instrumental Variable method. Assumption: M is known
% and matrices B and K are symmetric.
%
% WARNING: Transfer matrix H is the ACCELERANCE!
%
% Input:
% H: Transfer matrices as a function of omega
% omega: Frequencies
% M: The known mass matrix
%
% Output:
% X: Damping and stiffness matrices by means of IV
% Xleast: Damping and stiffness matrices calculated by means of Least Squares
% Hh: Modelled IV Transfer matrix
%
% By R.J.W. Knaapen, 1996

iter = 1;
count = 0;
maxiter = 25;
conv = 0;
err = 1E-4;

eltime = cputime;

% Startvalues using the Least Squares method:
[Xst,A,E, C] = LSquare3(H, omega, M);
Xleast = Xst;
[len,dim] = size(H);
n = len/dim;

while (iter==1) & (conv==0),

  count = count + 1;
  disp(count);

  % Extract the matrices from the estimation Xst:
  Xls = C*Xst;
  Bst = [];
  Kst = [];
  for i = 1:dim,
    Bst = [Bst; Xls((i-1)*dim+1:(i-1)*dim+dim)'];
    Kst = [Kst; Xls(dim^2+(i-1)*dim+1:dim^2+(i-1)*dim+dim)'];
  end;
```

```
% Calculation of IV Output Hh and construction of matrix V:
V = [];
Hh = [];
for i = 1:n,
  Hhi = inv(M-j/omega(i)*Bst-1/(omega(i)^2)*Kst);
  Hh = [Hh; Hhi];
  Z = zeros(2*dim*dim,dim*dim);
  for m = 1:dim,
    Z((m-1)*2*dim+1:(m-1)*2*dim+dim,       (m-1)*dim+1:(m-1)*dim+dim) = ...
      1/omega(i)*imag(Hhi);
    Z((m-1)*2*dim+dim+1:(m-1)*2*dim+2*dim, (m-1)*dim+1:(m-1)*dim+dim) = ...
     -1/omega(i)*real(Hhi);
    Z((m-1)*2*dim+1:(m-1)*2*dim+dim,       dim^2+(m-1)*dim+1:dim^2+(m-1)*dim+dim) = .
     -1/omega(i)^2*real(Hhi);
    Z((m-1)*2*dim+dim+1:(m-1)*2*dim+2*dim, dim^2+(m-1)*dim+1:dim^2+(m-1)*dim+dim) = .
     -1/omega(i)^2*imag(Hhi);
  end;
  V = [V; Z];
end;

if count==1,
  Hls=Hh;
end;

% Convergence test (wether iteration has proceeded sufficiently)
if count>1,
  X = Xst;
  dx = abs(max(max(Xst-Xprev)))/abs(max(max(Xprev)));
  if dx < err,
    conv = 1;
    message=['Matrices converged. Error: ' num2str(dx)];
  end;
  dH = abs(max(max(Hh-H)))/abs(max(max(H)));
  if dH < err,
    conv = 1;
    message=['Transfermatrix converged. Error: ' num2str(dH)];
  end;
  if count > maxiter,
    iter = 0;
    message='Maximum number of iterations reached.';
  end;
end;

% New estimation:
Xprev = Xst;
V = V*C;
```

```
  Xiv = inv(V.'*A)*V.'*E;
  Xst = Xiv;

end;

eltime = cputime - eltime;

disp(message);
disp(['Number of iterations: ' num2str(count-1) ' in ' num2str(eltime) ' seconds.']);
```

Appendix F

Numerical Results

F.1 Theoretical Stiffness Matrices

All of the following bearing stiffness matrices are calculated using the proper weight of the shaft as a radial preload of 24 [N].

NSK 6208 deep groove ball bearing, Axial preload = 427 [N]:

$$\begin{bmatrix} 0.2125 \cdot 10^9 & 0 & 0 & 0 & -0.1087 \cdot 10^7 & 0 \\ 0 & 0.2125 \cdot 10^9 & 0.4339 \cdot 10^6 & 0.1087 \cdot 10^7 & 0 & 0 \\ 0 & 0.4339 \cdot 10^6 & 0.1654 \cdot 10^8 & 0.4656 \cdot 10^4 & 0 & 0 \\ 0 & 0.1087 \cdot 10^7 & 0.4656 \cdot 10^4 & 0.7517 \cdot 10^4 & 0 & 0 \\ -0.1087 \cdot 10^7 & 0 & 0 & 0 & 0.7516 \cdot 10^4 & 0 \\ 0 & 0 & 0 & 0 & 0 & 0 \end{bmatrix}$$

NSK 6208 deep groove ball bearing, Axial preload = 701 [N]:

$$\begin{bmatrix} 0.2388 \cdot 10^9 & 0 & 0 & 0 & -0.1381 \cdot 10^7 & 0 \\ 0 & 0.2388 \cdot 10^9 & 0.3740 \cdot 10^6 & 0.1381 \cdot 10^7 & 0 & 0 \\ 0 & 0.3740 \cdot 10^6 & 0.2386 \cdot 10^8 & 0.4601 \cdot 10^4 & 0 & 0 \\ 0 & 0.1381 \cdot 10^7 & 0.4601 \cdot 10^4 & 0.1084 \cdot 10^5 & 0 & 0 \\ -0.1381 \cdot 10^7 & 0 & 0 & 0 & 0.1084 \cdot 10^5 & 0 \\ 0 & 0 & 0 & 0 & 0 & 0 \end{bmatrix}$$

NSK 6208 deep groove ball bearing, Axial preload = 1422 [N]:

$$\begin{bmatrix} 0.2811 \cdot 10^9 & 0 & 0 & 0 & -0.1936 \cdot 10^7 & 0 \\ 0 & 0.2811 \cdot 10^9 & 0.2985 \cdot 10^6 & 0.1936 \cdot 10^7 & 0 & 0 \\ 0 & 0.2985 \cdot 10^6 & 0.4014 \cdot 10^8 & 0.4497 \cdot 10^4 & 0 & 0 \\ 0 & 0.1936 \cdot 10^7 & 0.4497 \cdot 10^4 & 0.1824 \cdot 10^5 & 0 & 0 \\ -0.1936 \cdot 10^7 & 0 & 0 & 0 & 0.1824 \cdot 10^5 & 0 \\ 0 & 0 & 0 & 0 & 0 & 0 \end{bmatrix}$$

NSK 6208 deep groove ball bearing, Axial preload = 1721 [N]:

$$\begin{bmatrix} 0.2935 \cdot 10^9 & 0 & 0 & 0 & -0.2118 \cdot 10^7 & 0 \\ 0 & 0.2935 \cdot 10^9 & 0.2799 \cdot 10^6 & 0.2118 \cdot 10^7 & 0 & 0 \\ 0 & 0.2799 \cdot 10^6 & 0.4616 \cdot 10^8 & 0.4462 \cdot 10^4 & 0 & 0 \\ 0 & 0.2118 \cdot 10^7 & 0.4462 \cdot 10^4 & 0.2098 \cdot 10^5 & 0 & 0 \\ -0.2118 \cdot 10^7 & 0 & 0 & 0 & 0.2098 \cdot 10^5 & 0 \\ 0 & 0 & 0 & 0 & 0 & 0 \end{bmatrix}$$

RPF 7208 angular contact bearing, Axial preload = 445 [N]:

$$\begin{bmatrix} 0.6729 \cdot 10^8 & 0 & 0 & 0 & -0.1714 \cdot 10^7 & 0 \\ 0 & 0.6940 \cdot 10^8 & -0.1764 \cdot 10^6 & 0.1762 \cdot 10^7 & 0 & 0 \\ 0 & -0.1764 \cdot 10^6 & 0.9993 \cdot 10^8 & 0.1272 \cdot 10^6 & 0 & 0 \\ 0 & 0.1762 \cdot 10^7 & 0.1272 \cdot 10^6 & 0.4602 \cdot 10^5 & 0 & 0 \\ -0.1714 \cdot 10^7 & 0 & 0 & 0 & 0.4464 \cdot 10^5 & 0 \\ 0 & 0 & 0 & 0 & 0 & 0 \end{bmatrix}$$

RPF 7208 angular contact bearing, Axial preload = 852 [N]:

$$\begin{bmatrix} 0.8386 \cdot 10^8 & 0 & 0 & 0 & -0.2149 \cdot 10^7 & 0 \\ 0 & 0.8438 \cdot 10^8 & -0.1444 \cdot 10^6 & 0.2161 \cdot 10^7 & 0 & 0 \\ 0 & -0.1444 \cdot 10^6 & 0.1259 \cdot 10^9 & 0.8519 \cdot 10^5 & 0 & 0 \\ 0 & 0.2161 \cdot 10^7 & 0.8519 \cdot 10^5 & 0.5727 \cdot 10^5 & 0 & 0 \\ -0.2149 \cdot 10^7 & 0 & 0 & 0 & 0.5693 \cdot 10^5 & 0 \\ 0 & 0 & 0 & 0 & 0 & 0 \end{bmatrix}$$

RPF 7208 angular contact bearing, Axial preload = 1262 [N]:

$$\begin{bmatrix} 0.9512 \cdot 10^8 & 0 & 0 & 0 & -0.2449 \cdot 10^7 & 0 \\ 0 & 0.9533 \cdot 10^8 & -0.1283 \cdot 10^6 & 0.2453 \cdot 10^7 & 0 & 0 \\ 0 & -0.1283 \cdot 10^6 & 0.1451 \cdot 10^9 & 0.6613 \cdot 10^5 & 0 & 0 \\ 0 & 0.2453 \cdot 10^7 & 0.6613 \cdot 10^5 & 0.6587 \cdot 10^5 & 0 & 0 \\ -0.2449 \cdot 10^7 & 0 & 0 & 0 & 0.6573 \cdot 10^5 & 0 \\ 0 & 0 & 0 & 0 & 0 & 0 \end{bmatrix}$$

RPF 7208 angular contact bearing, Axial preload = 1706 [N]:

$$\begin{bmatrix} 0.1046 \cdot 10^9 & 0 & 0 & 0 & -0.2702 \cdot 10^7 & 0 \\ 0 & 0.1047 \cdot 10^9 & -0.1180 \cdot 10^6 & 0.2704 \cdot 10^7 & 0 & 0 \\ 0 & -0.1180 \cdot 10^6 & 0.1620 \cdot 10^9 & 0.5438 \cdot 10^5 & 0 & 0 \\ 0 & 0.2704 \cdot 10^7 & 0.5438 \cdot 10^5 & 0.7353 \cdot 10^5 & 0 & 0 \\ -0.2702 \cdot 10^7 & 0 & 0 & 0 & 0.7346 \cdot 10^5 & 0 \\ 0 & 0 & 0 & 0 & 0 & 0 \end{bmatrix}$$

F.2 Theoretical Transfer Functions

This appendix contains all modelled transfer functions in the axial preloaded case combined with the proper weight of the shaft as radial preload in y-direction.

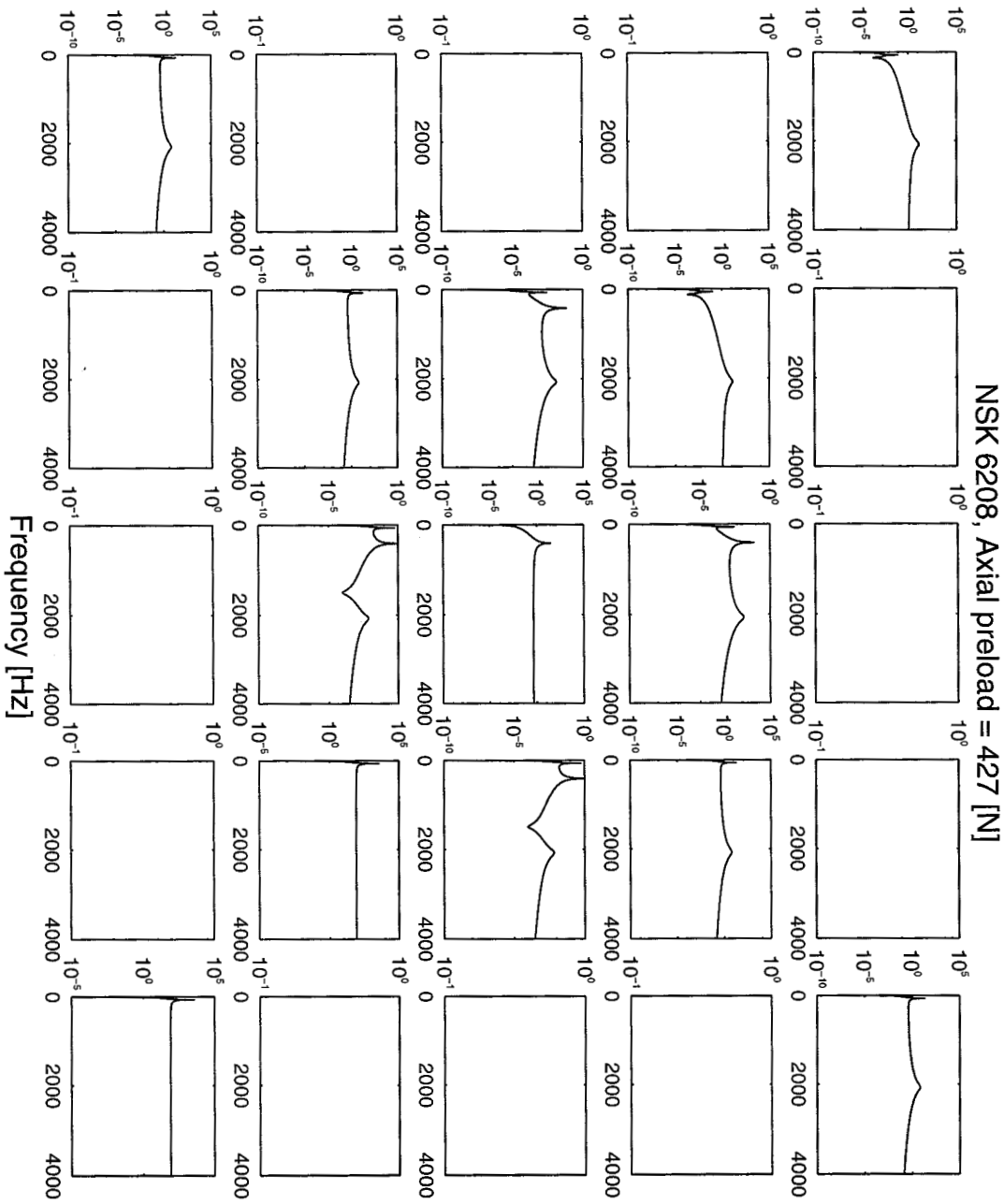

Figure~F.1: Theoretical transfer function. Axial preload = 427 $[N]$ (NSK 6208)

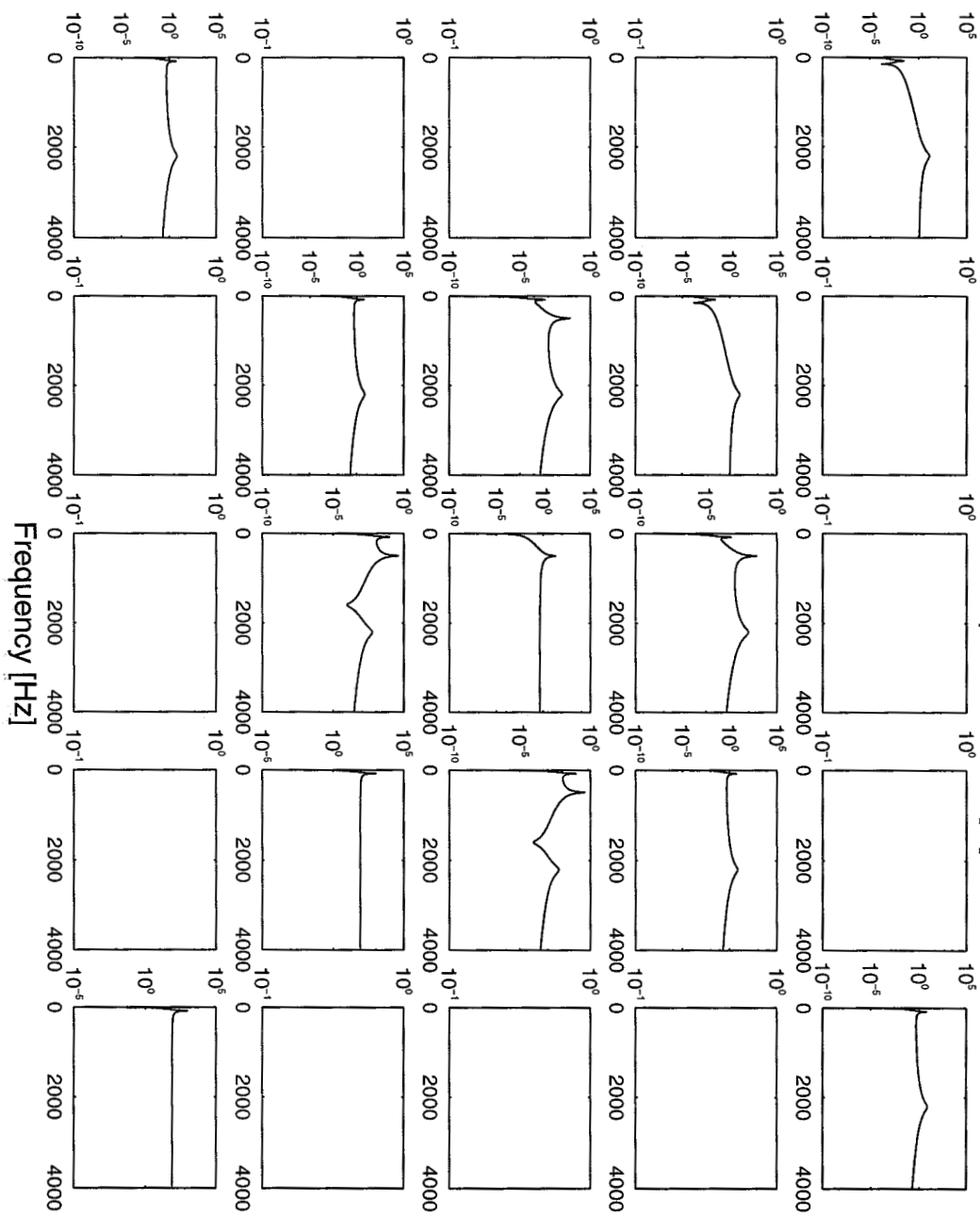

Figure~F.2: Theoretical transfer function. Axial preload = 701 $[N]$ (NSK 6208)

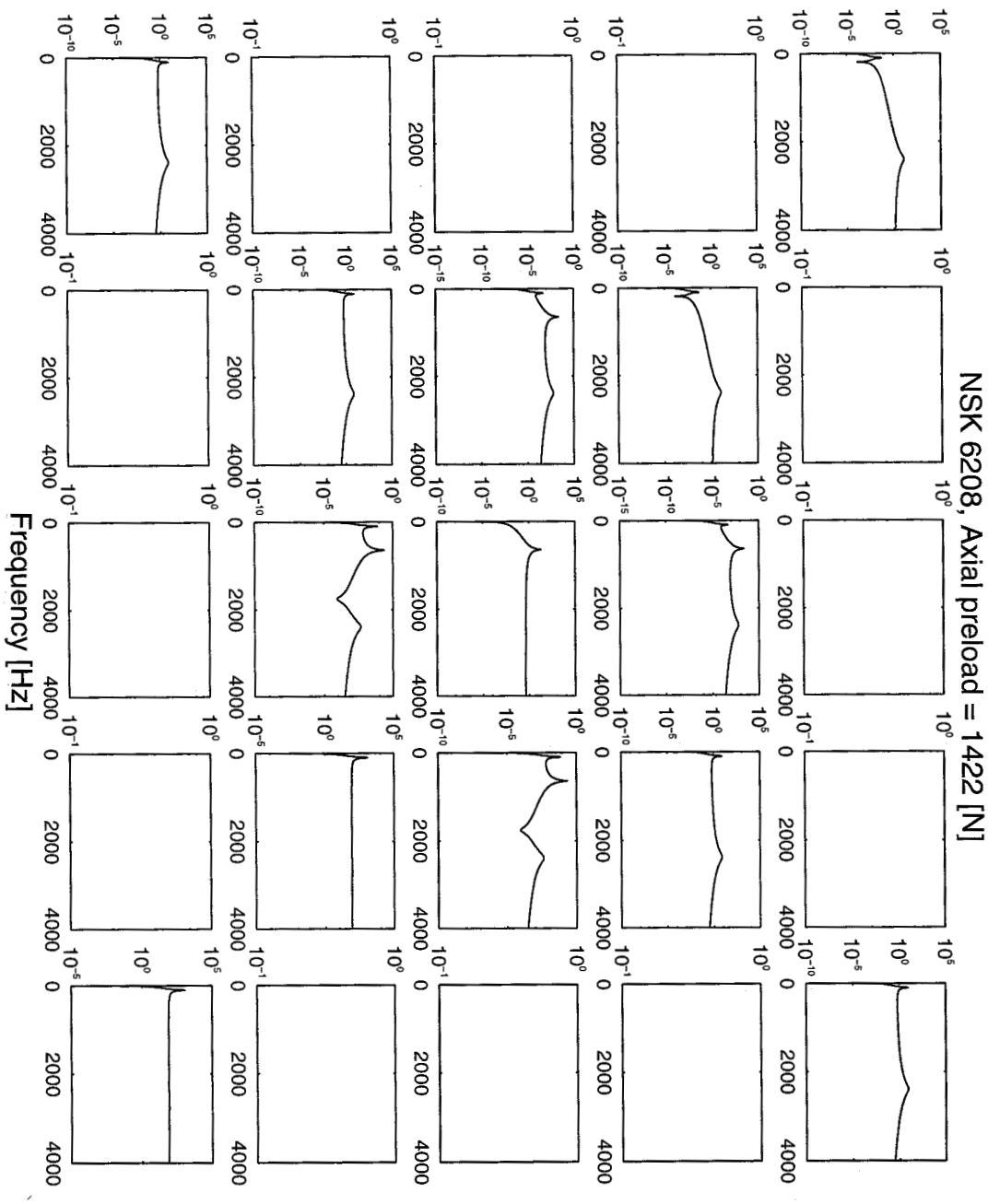

Figure~F.3: Theoretical transfer function. Axial preload = 1422 $[N]$ (NSK 6208)

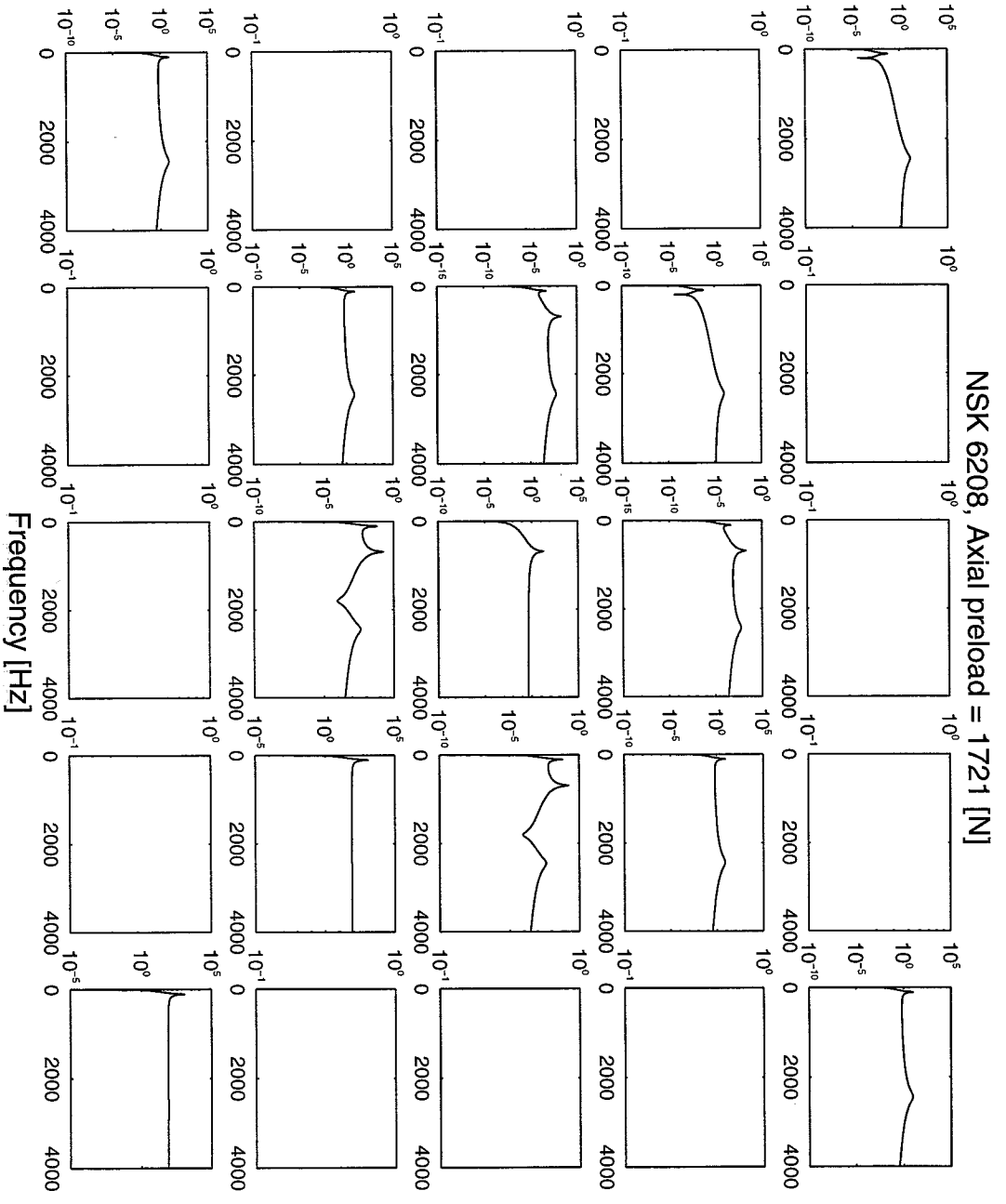

Figure~F.4: Theoretical transfer function. Axial preload = 1721 [N] (NSK 6208)

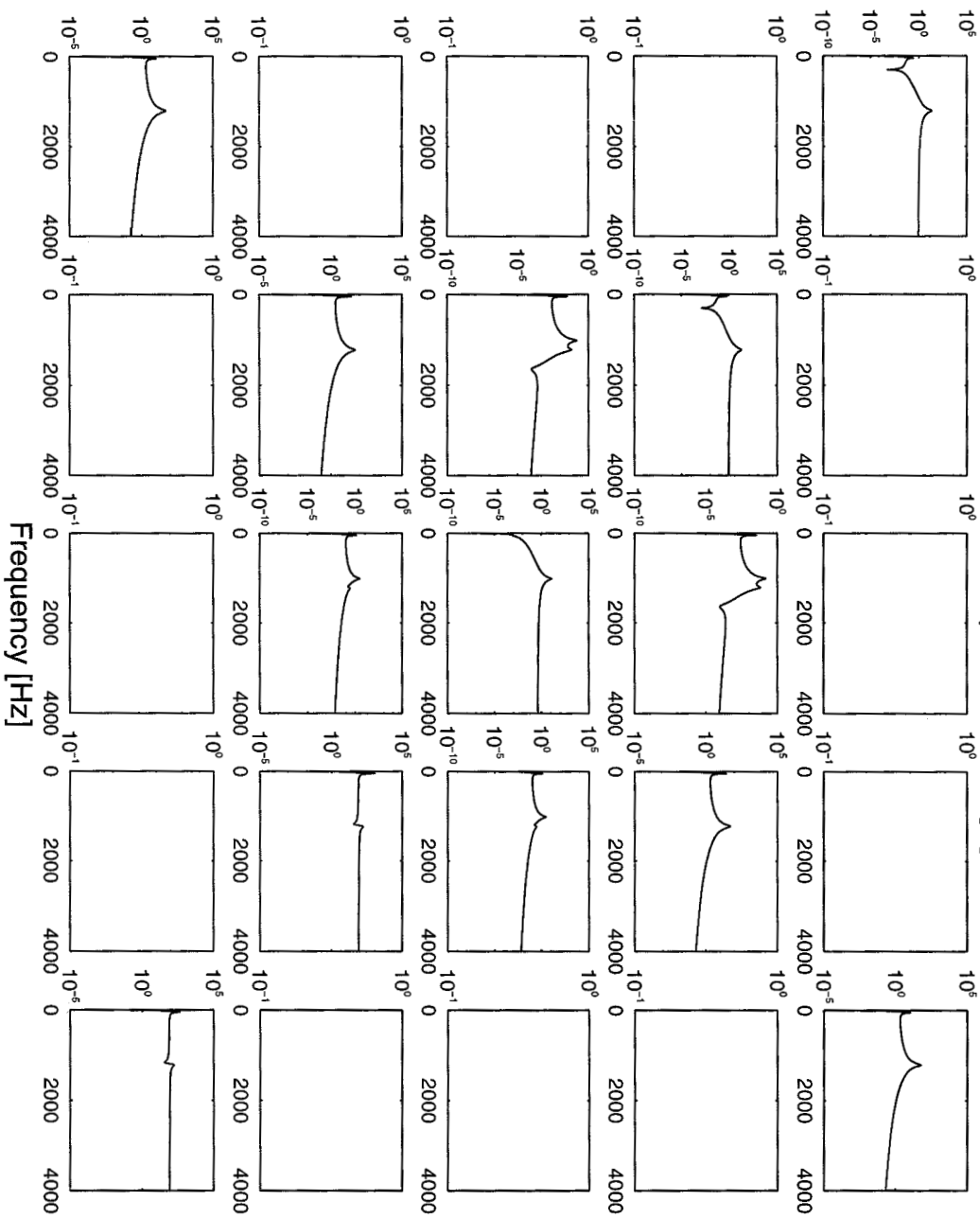

Figure~F.5: Theoretical transfer function. Axial preload = 445 $[N]$ (RPF 7208)

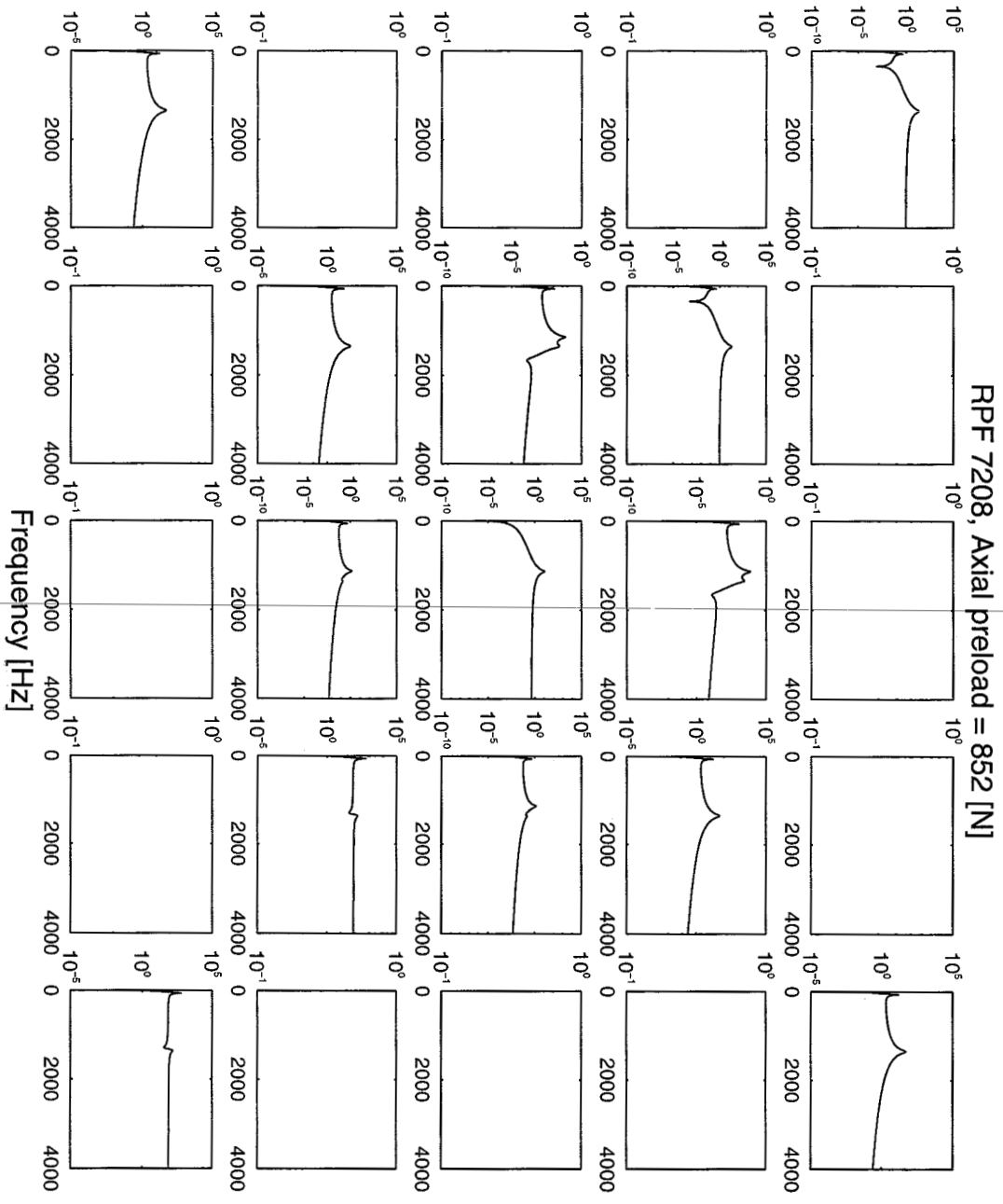

Figure~F.6: Theoretical transfer function. Axial preload = 852 $[N]$ (RPF 7208)

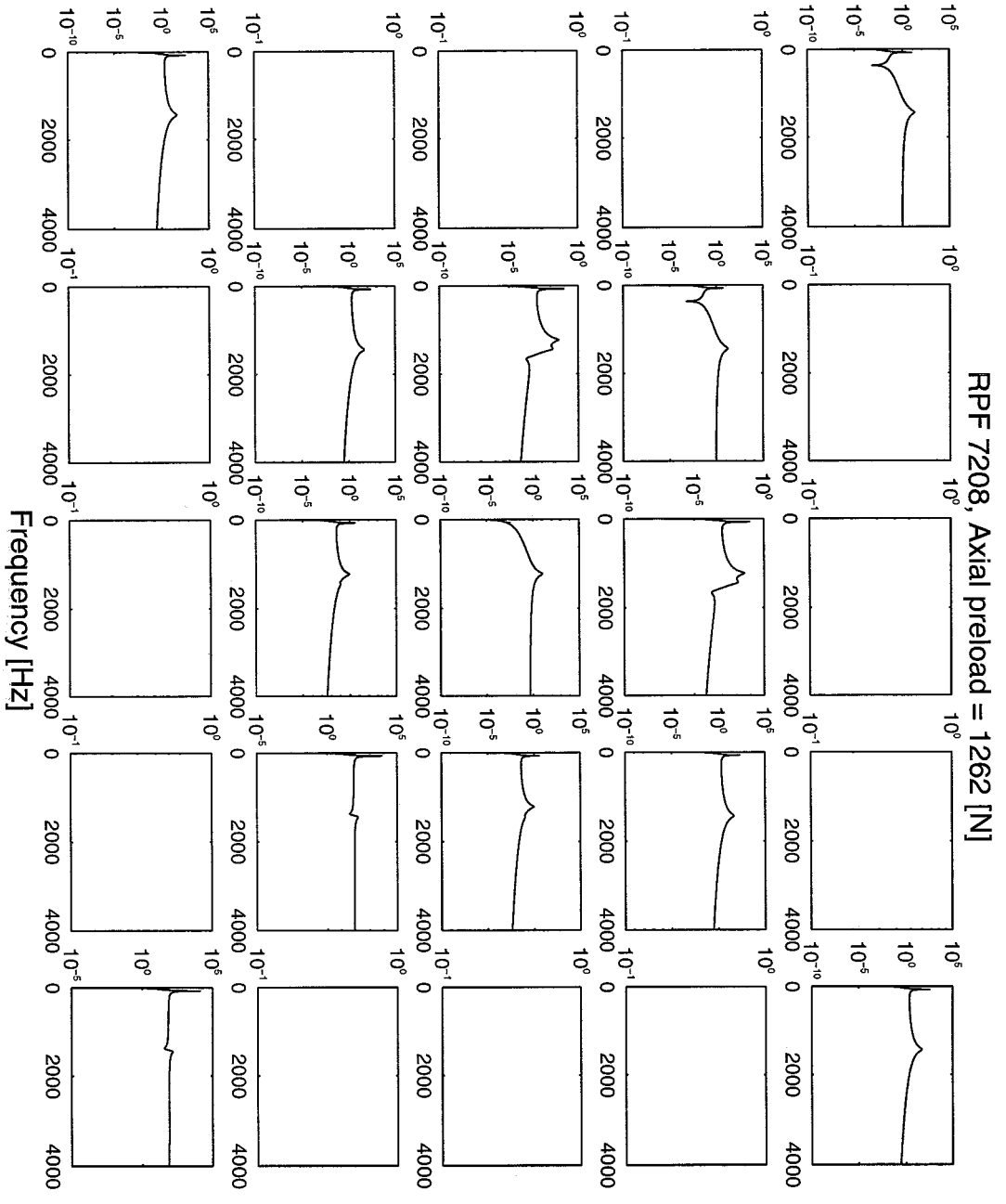

Figure~F.7: Theoretical transfer function. Axial preload = 1262 $[N]$ (RPF 7208)

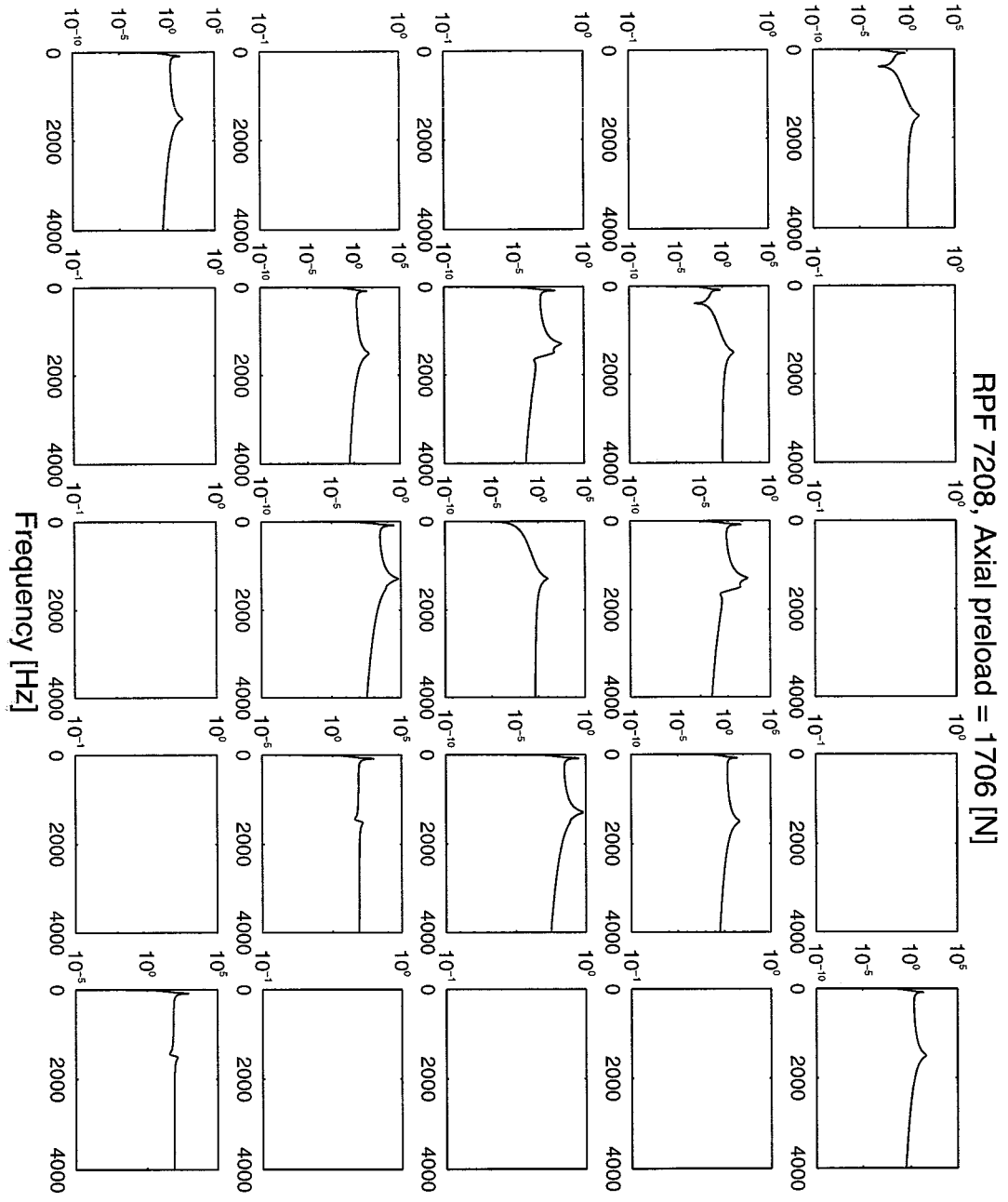

Figure~F.8: Theoretical transfer function. Axial preload = 1706 $[N]$ (RPF 7208)

F.3 Measured Transfer Functions

In this appendix, all measured transfer matrices (straight lines) are printed together with the modelled transfer functions (dotted lines). The preload, in each case, is a combination of the applied axial preload combined with the proper weight of the shaft.

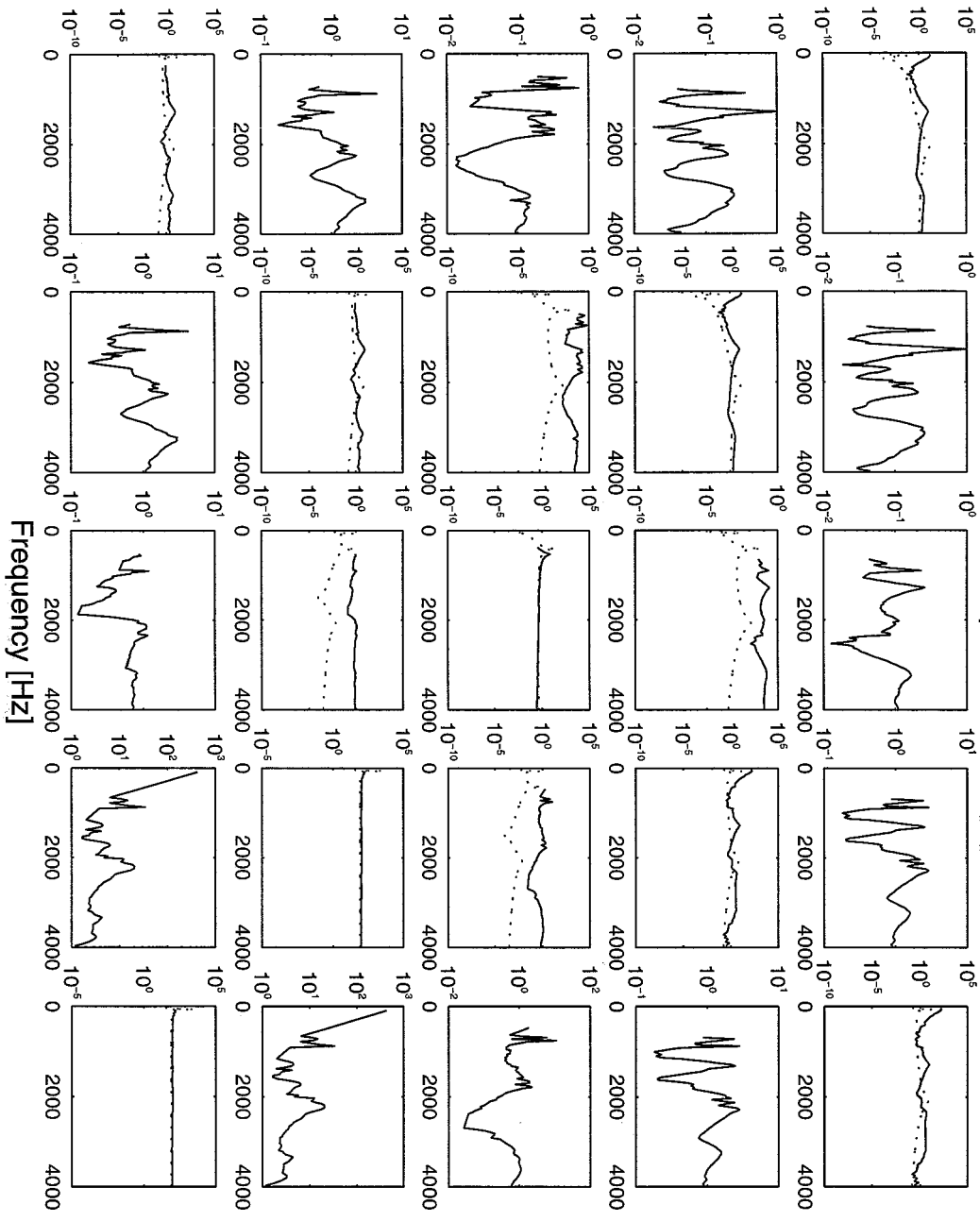

Figure~F.9: Measured (-) and theoretical (...) transfer function. Axial preload = 427 $[N]$ (NSK 6208)

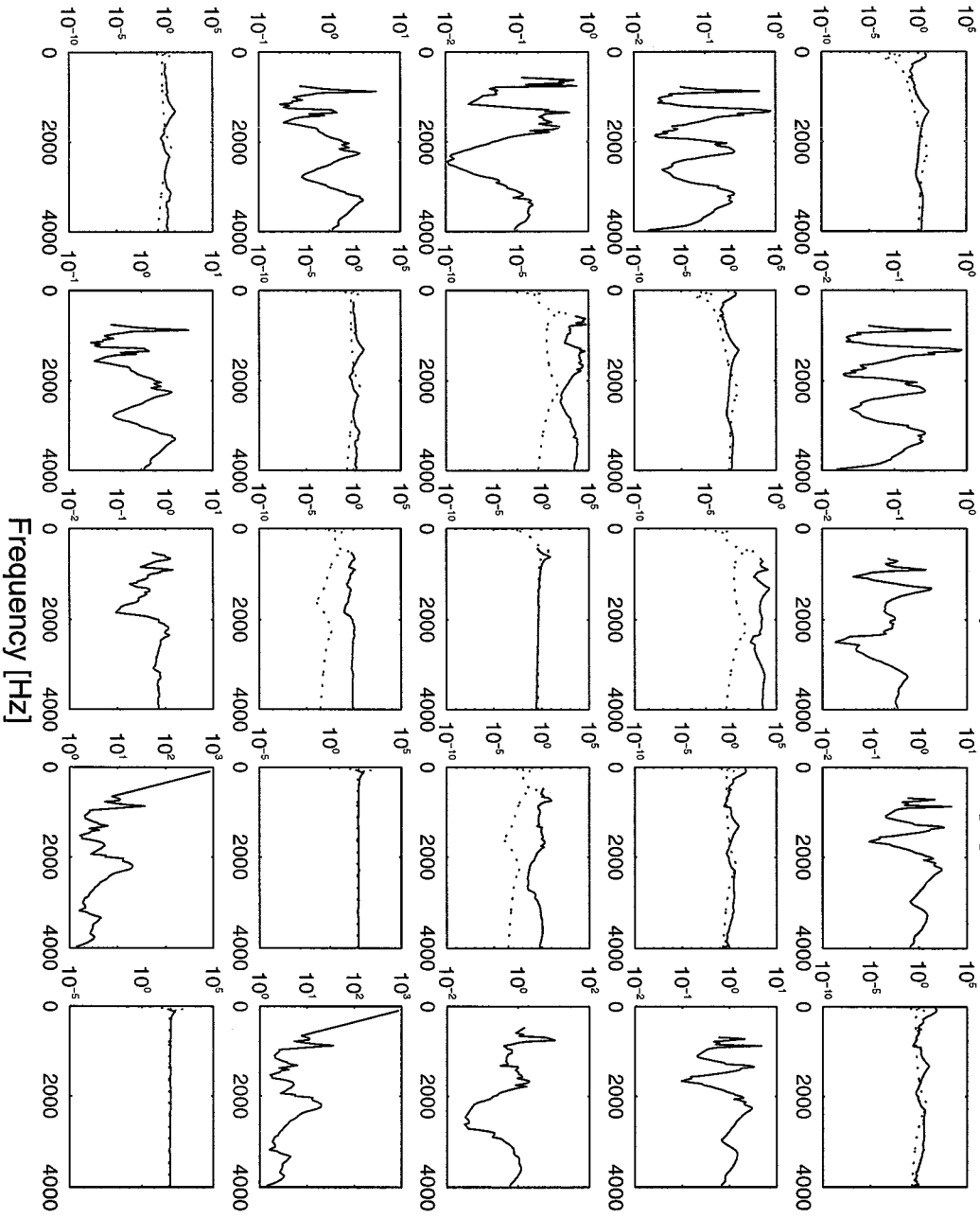

Figure~F.10: Measured (-) and theoretical (...) transfer function. Axial preload = 701 $[N]$ (NSK 6208)

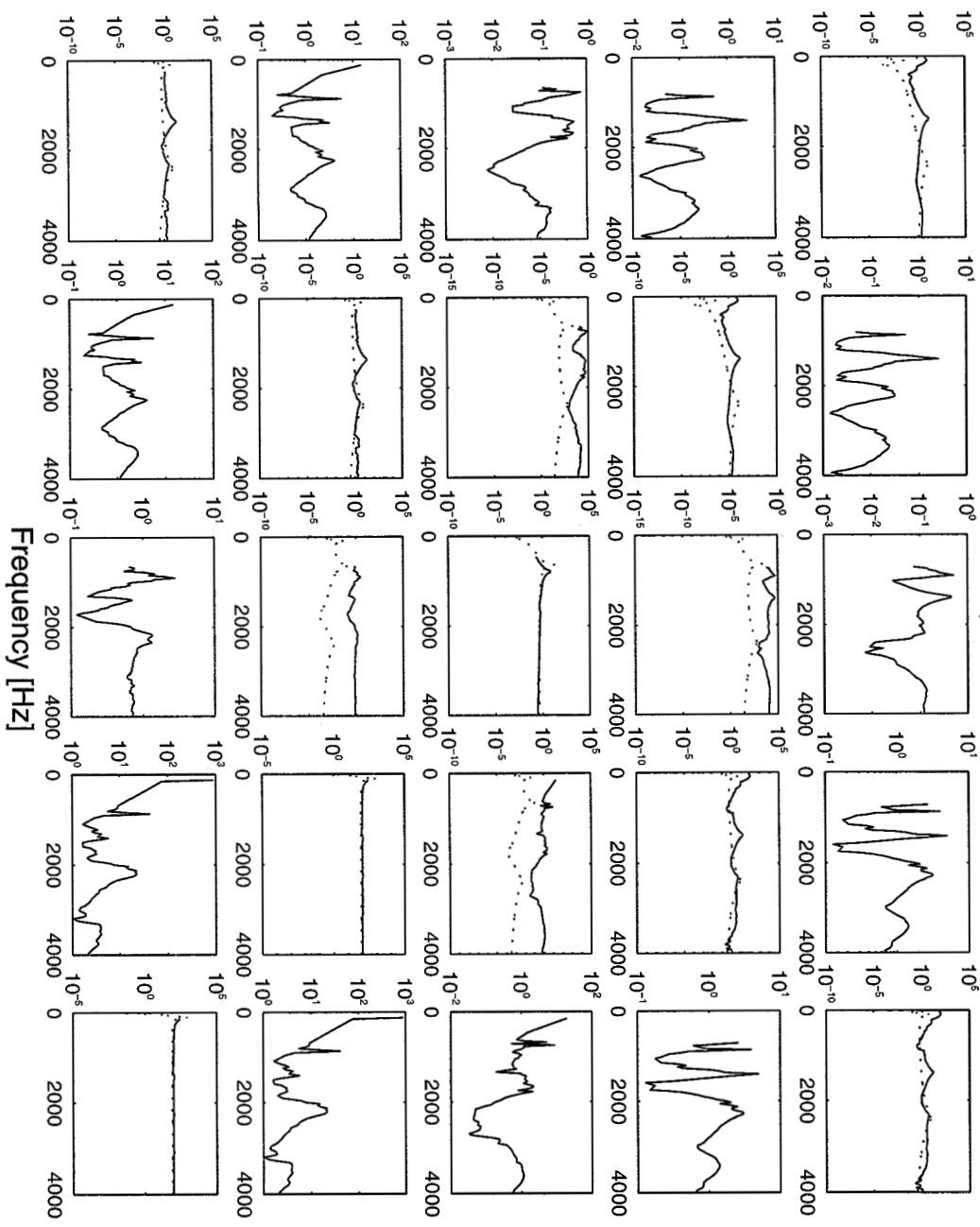

Figure~F.11: Measured (-) and theoretical (...) transfer function. Axial preload = 1422 $[N]$ (NSK 6208)

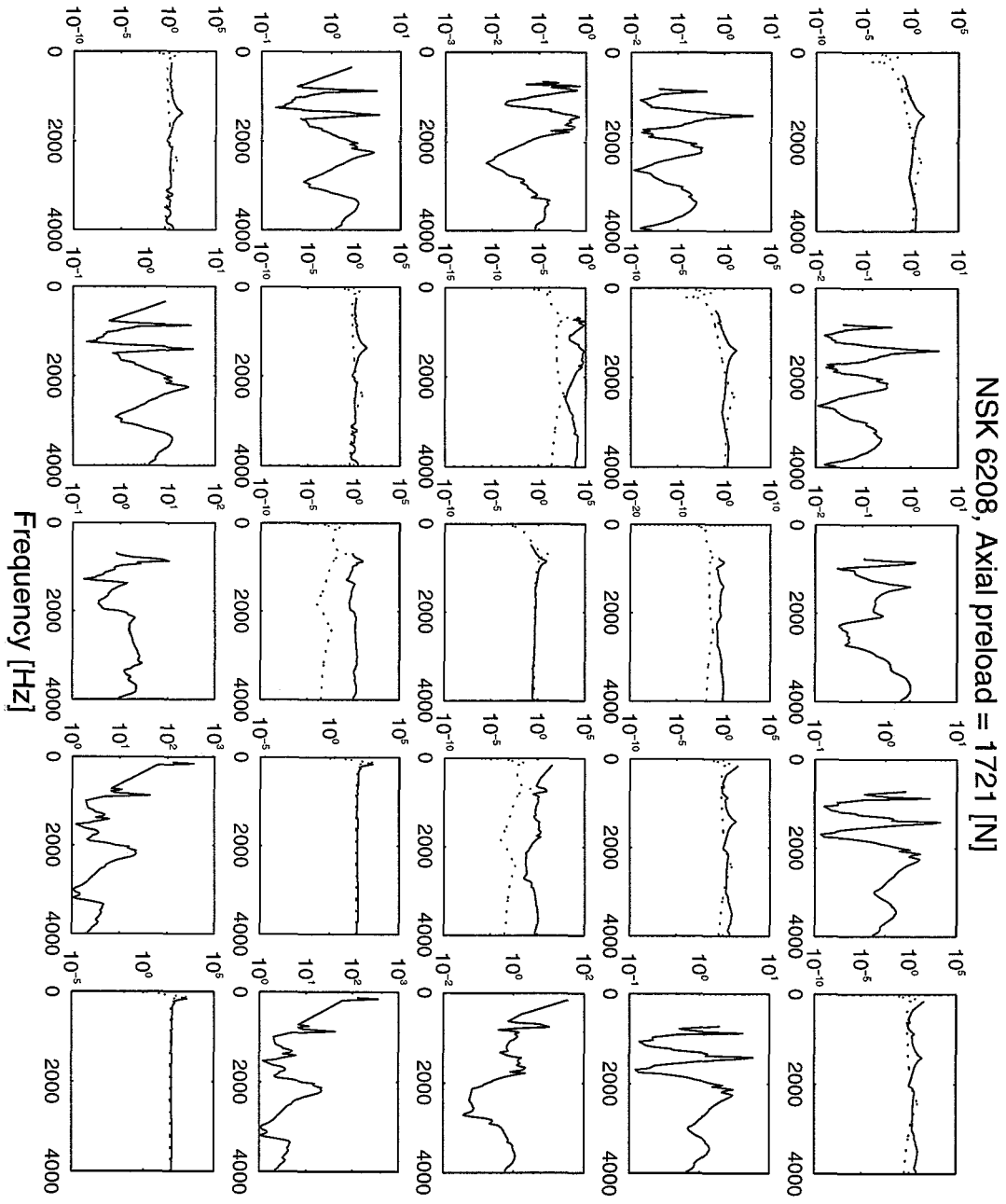

Figure~F.12: Measured (-) and theoretical (...) transfer function. Axial preload = 1721 $[N]$ (NSK 6208)

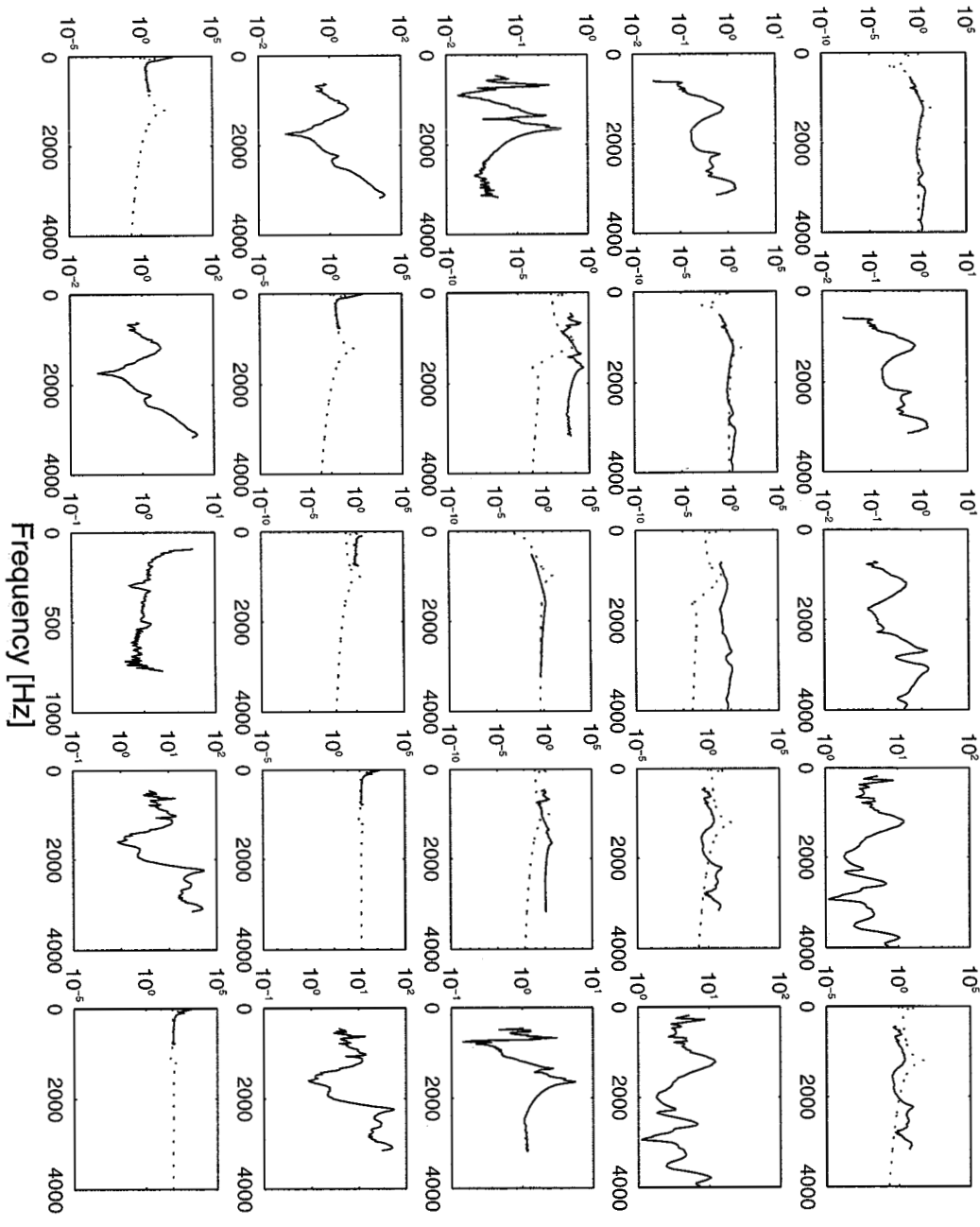

Figure~F.13: Measured (-) and theoretical (...) transfer function. Axial preload = 445 $[N]$ (RPF 7208)

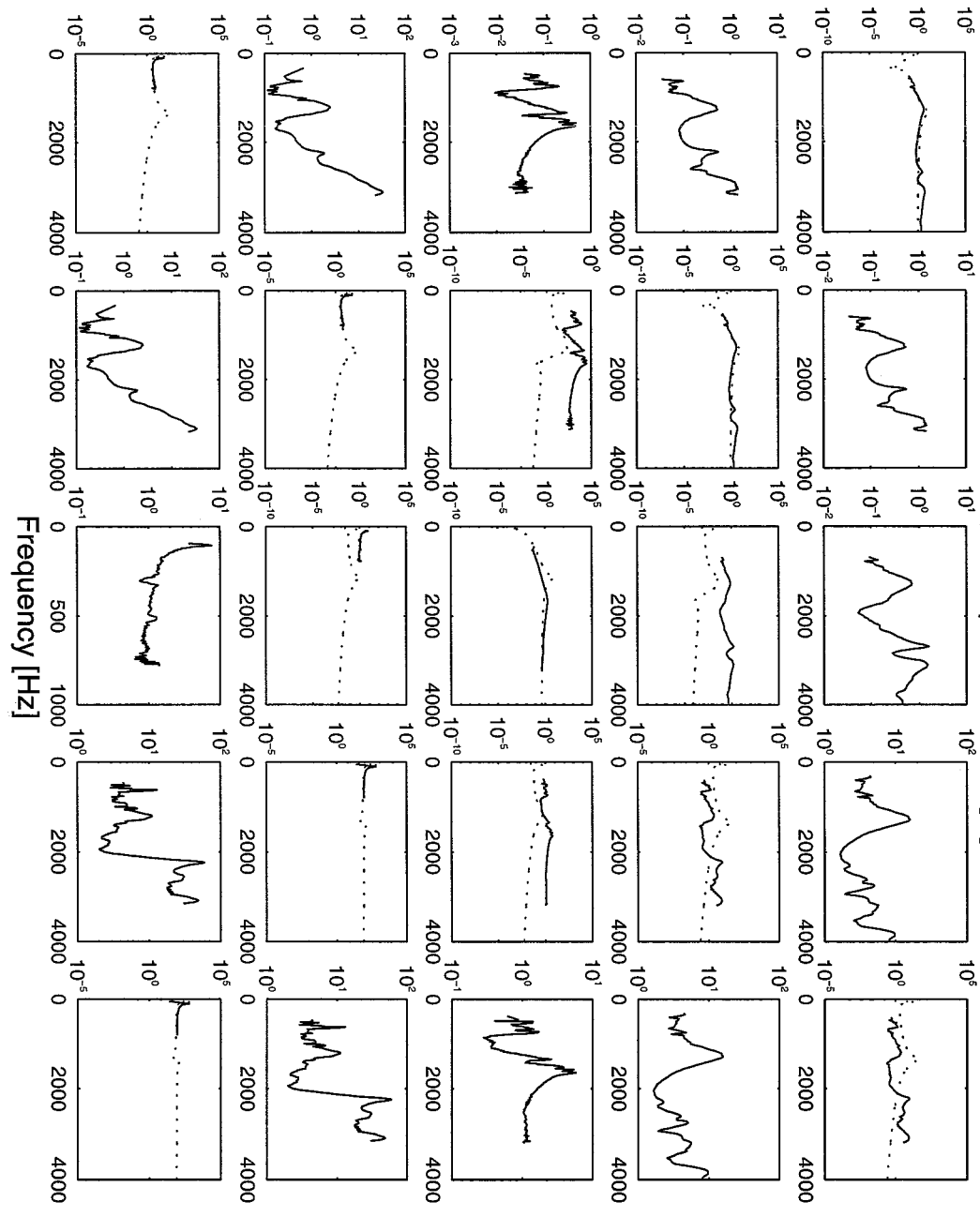

Figure~F.14: Measured (-) and theoretical (...) transfer function. Axial preload = 852 $[N]$ (RPF 7208)

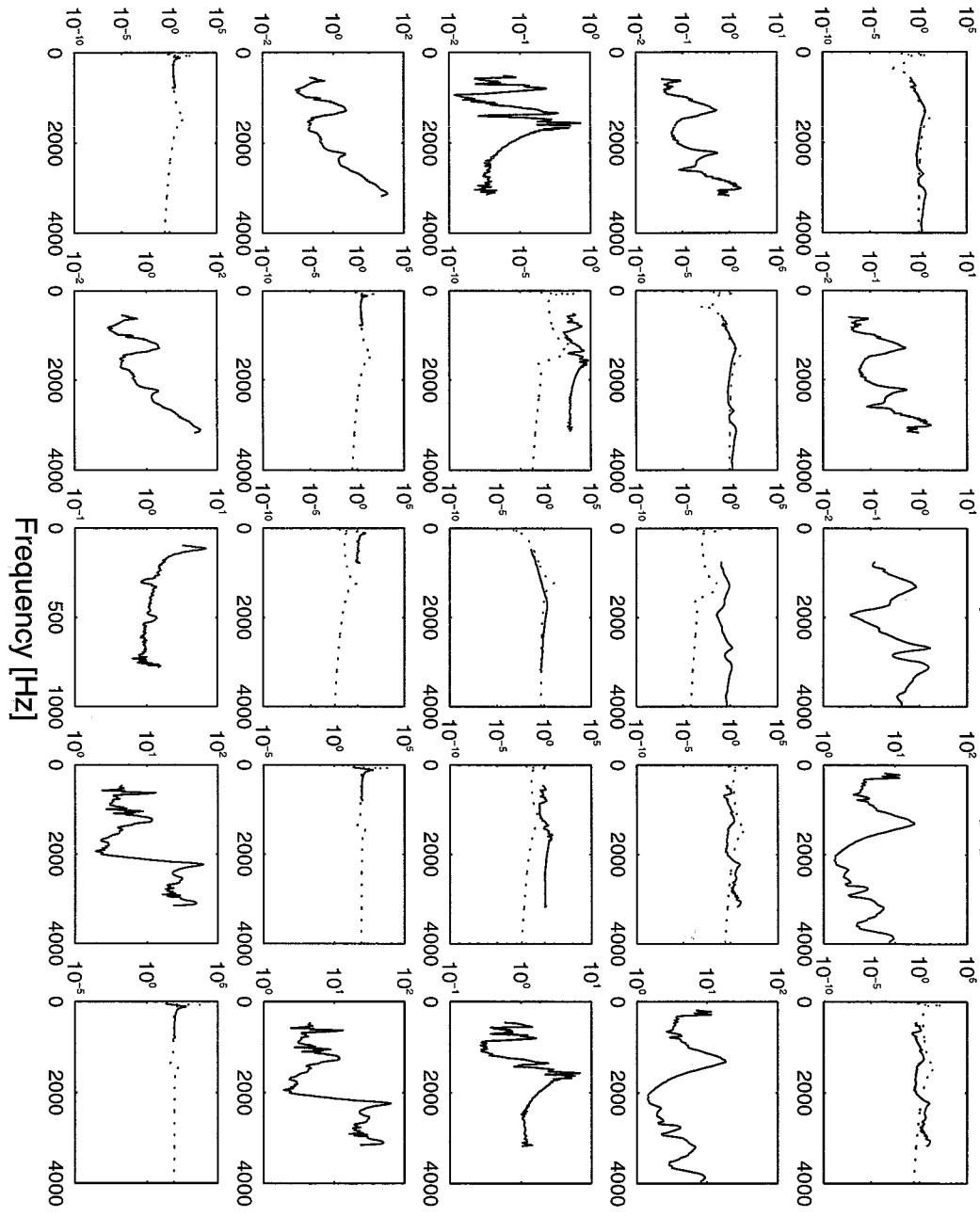

Figure~F.15: Measured (-) and theoretical (...) transfer function. Axial preload = 1262 $[N]$ (RPF 7208)

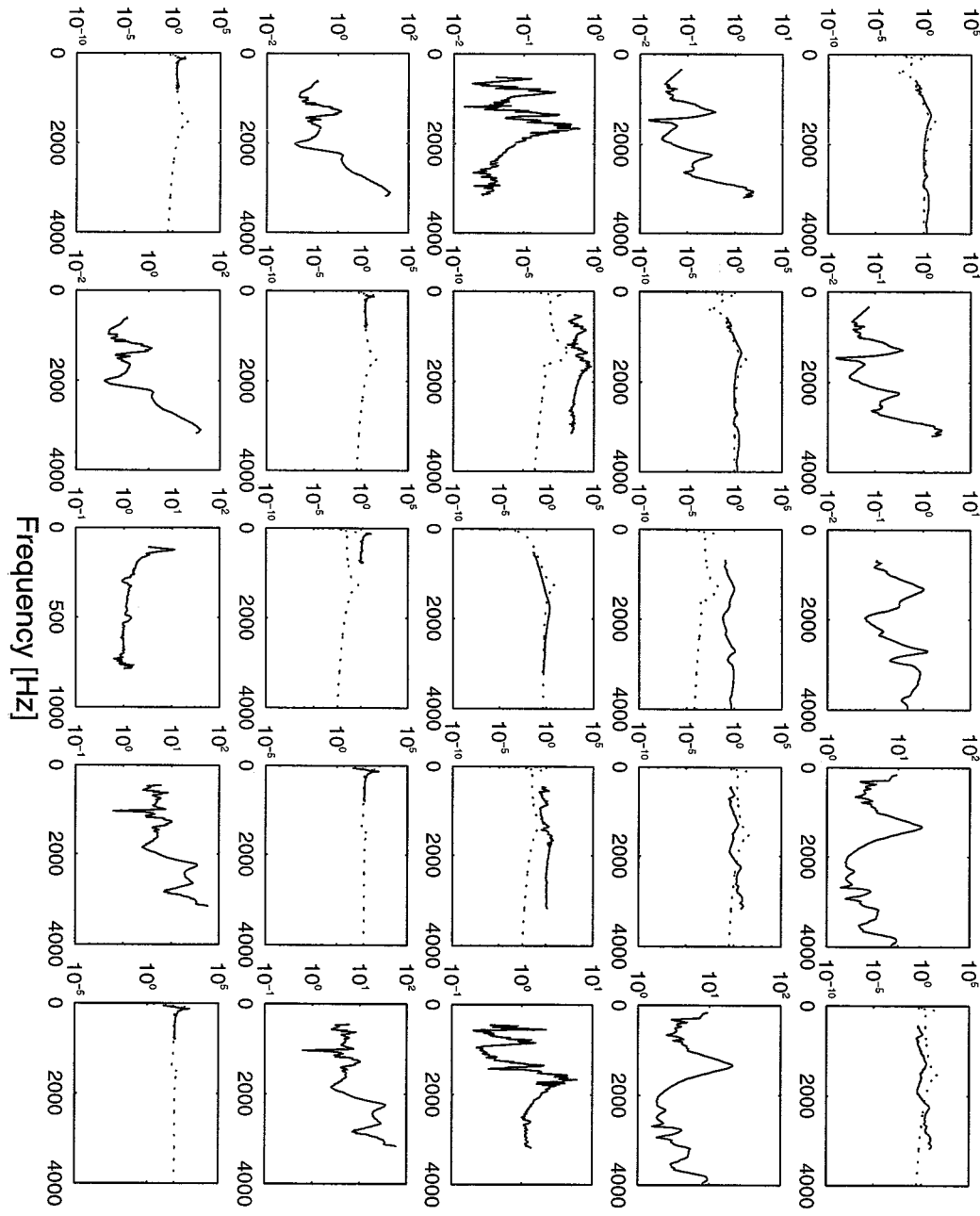

Figure~F.16: Measured (-) and theoretical (...) transfer function. Axial preload = 1706 $[N]$ (RPF 7208)

Bibliography

[1] Lim, T.C. and Singh, R. (1990): *Vibration transmission through rolling element bearings in geared rotor systems*, NASA contractor report 4334, Ohio State University, Ohio, USA.

[2] Staps, E. (1995): *Identificatiemethodieken ter bepaling van de stijfheidsmatrix van wentellagers*, WFW rapport 95.077, Eindhoven University of Technology, Eindhoven, The Netherlands.

[3] Heuvelmans, D.F.J.M. (1993): *Experimentele verificatie van de stijfheidsmatrix van wentellagers*, WFW rapport 93.145, Eindhoven University of Technology, Eindhoven, The Netherlands.

[4] Roosmalen, A.N.J. van (1994): *Design tools for low noise gear transmissions*, Ph.D. thesis, Faculty of Mechanical Engineering, Power Transmissions and Tribology Laboratory, Eindhoven University of Technology, Eindhoven, The Netherlands.

[5] Schroën, H.G.M. (1990): *Lager, Verwerking van een mathematisch lagermodel tot het computerprogramma Lager*, NOVEM-project "Geluidarme tandwieloverbrengingen", Eindhoven University of Technology, Eindhoven, The Netherlands.

[6] Rinawi, A.M. and Clough, R.W. (1991): *Improved amplitude fitting for frequency and damping estimation*, University of Berkeley, USA.

[7] Kraus, J.; Blech, J.J. and Braun, S.G. (1987): *In Situ determination of rolling bearing stiffness and damping by modal analysis*, Journal of Vibration, Acoustics, Stress and Reliability in Design **109**, 235-240, Faculty of Mechanical Engineering, Technion-Israel Institute of Technology, Haifa, Israel.

[8] Rigaud, E. and Sabot, J. (1996): *Effect of elasticity of shafts, bearings, casing and couplings on the critical rotational speeds of a gearbox*, VDI Berichte **1230**, 833-845, Ecully, France.

[9] Dietl, P.; Zeillinger, R.; Springer, H. (1996): *Experimentelle Identifikation und Berechnung des Dämpfungsvermögens von Kugellagern*, VDI Berichte **1285**, 259-273, Vienna, Austria.

[10] Rook, T.E. and Singh, R. (1996): *Mobility analysis of structure borne noise power flow through bearings in gearbox-like structures*, Noise Control Engineering Journal **44 (2)**, 69-78, Acoustics & Dynamics Laboratory, Department of Mechanical Engineering, Ohio State University, Columbus, Ohio, USA.

[11] Tiwari, R. and Vyas, N.S. (1995): *Estimation of non-linear stiffness parameters of rolling element bearings from random response of rotor-bearing systems*, Journal of Sound and Vibration **187 (2)**, 229-239, Department of Mechanical Engineering, Indian Institute of Technology, Kampur, India.

[12] Kraker, A. de (1992): *Numeriek-experimentele analyse van dynamische systemen*, Collegedictaat 4668, Eindhoven University of Technology, Eindhoven, The Netherlands.

[13] Young, P.C. (1969): *An instrumental variable method for real-time identification of a noisy process*, Automatica **6**, 271-287, Department of Engineering, University of Cambridge, England.

[14] Young, P.C. (1984): *Recursive estimation and time-series analysis*, Springer-Verlag Berlin Heidelberg New York Tokyo.

[15] Dortmans, L.J.M.G. (1988): *Aspects of the dynamic behaviour of the human knee joint*, Ph.D. thesis, Faculty of Mechanical Engineering, Eindhoven University of Technology, Eindhoven, The Netherlands.